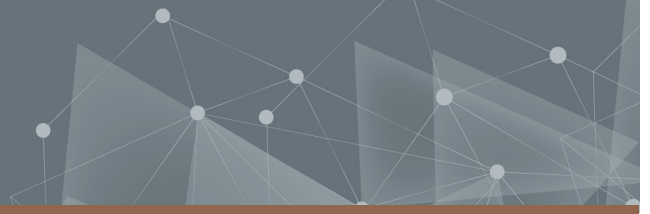




CHALMERS
UNIVERSITY OF TECHNOLOGY



La_{2-x}Sr_xCuO₄ thin films and nanostructures to study local ordering phenomena in a striped superconductor

Master's Thesis in Microtechnology and Nanoscience

MARCO BIAGI

DEPARTMENT OF MICROTECHNOLOGY AND NANOSCIENCE

CHALMERS UNIVERSITY OF TECHNOLOGY
Gothenburg, Sweden 2022
www.chalmers.se

MASTER'S THESIS 2022

**$\text{La}_{2-x}\text{Sr}_x\text{CuO}_4$ thin films and nanostructures to
study local ordering phenomena in a striped
superconductor**

MARCO BIAGI



CHALMERS
UNIVERSITY OF TECHNOLOGY

Department of Microtechnology and nanoscience

QManD

CHALMERS UNIVERSITY OF TECHNOLOGY

Gothenburg, Sweden 2022

La_{2-x}Sr_xCuO₄ thin films and
nanostructures to study local ordering phenomena in a striped superconductor
MARCO BIAGI

© MARCO BIAGI, 2022.

Supervisor: Riccardo Arpaia
Examiner: Alexei Kalaboukhov

Master's Thesis 2022
Department of Microtechnology and nanoscience
QManD
Chalmers University of Technology
SE-412 96 Gothenburg
Telephone +46 31 772 1000

Typeset in L^AT_EX
Printed by Chalmers Reproservice
Gothenburg, Sweden 2022

Abstract

Since their discovery in 1986, cuprates high critical temperature superconductors (HTS) represent one of the most fascinating class of materials in condensed matter physics. Understanding the underlying mechanism behind high- T_c superconductivity is a real challenge, which could results in the possibility to design in the future a room-temperature superconductor, a technological holy grail allowing an energy-efficiency revolution, and the large-scale realization of applications such as magnetically levitated trains and quantum computers. The strong electron-electron correlations in HTS lead to the formation of exotic charge and spin orders such as charge density waves (CDW) and spin density waves (SDW), that are respectively charge and spin density periodic spatial modulations. In La-based cuprates, as $\text{La}_{2-x}\text{Sr}_x\text{CuO}_4$ (LSCO), CDW and SDW are characterized, in a well-defined portion of the phase diagram, by a well-defined relation of periodicity, forming the so-called stripe order. The understanding of these local orders is crucial, since they have been recently reported to be responsible for the superconducting and normal state of HTS. Their nature can be effectively investigated in thin films, where the strain induced by the substrate, and the confinement of the HTS at the nanoscale, have been proven to be two powerful knobs to manipulate these orders and understand their mutual interaction. The fabrication of HTS nanostructures is a very challenging task, and up to now relevant results were obtained mainly for $\text{YBa}_2\text{Cu}_3\text{O}_{7-\delta}$. We optimized the growth of 20 nm thick optimally doped LSCO thin films on LaSrAlO_4 (001) substrates by Pulsed Laser Deposition. The films are smooth, as confirmed by atomic force microscopy and reflection high-energy electron diffraction, and highly crystalline, as confirmed by X-ray diffraction. Our best films show a $T_c \sim 39$ K, comparable to the bulk value. Finally, we realize LSCO nanowires down to 50 nm width. We measure their J_c values and study the $J_c(T)$. To prove the high degree of homogeneity of our nanowires, we compare the value of J_c^0 , obtained by fitting the $J_c(T)$ with the Bardeen expression, to the Ginzburg-Landau theoretical limit for the depairing current J_v , due to vortex motion. Our results pave the way for the study of LSCO ground state at the nanoscale.



Acknowledgement

When I first arrived in Sweden I never imagined that I would have missed it once finished with my thesis. The reason is all the people who have contributed directly, or indirectly, to make this experience so amazing.

First of all, I want to thank my Politecnico di Milano supervisor Prof. Giacomo Ghiringhelli, without him none of this would have been possible, and Floriana Lombardi, the QManD group leader, that welcomed me in the group and always made me feel part of it, as if I had always been there.

Then, a huge thanks goes to the others members and friends of QManD and QDP: Xavier, The Kiryl (the sexiest guy of MC2), Eric, Vittorio, Kornelia, Roselle, Richa, Adythia, Lars, Munis, Bing, and Nah. It has been great to share all those moments with you, the fikas, the barbecues, the shuffleboard... I will never forget them.

Many thanks go also to all the cleanroom staff, in particular Henrik, who was always present in case of help or doubts with the tools.

Dulcis in fundo, I want to reserve special acknowledgments to special people.

To Alexei Kalaboukhov, my supervisor at Chalmers. You really taught me a lot, and you inspired me every day. The passion you have for science is just inexpressible, and if now I love physics even more than when I started it is also thank to you. I was lucky to have you as a mentor.

To all the master students who were with me along the way: Thijs, with your cheese-cucumber sandwich you really made me realize how lucky I am in eating Italian food, but I'll miss it in the end; Feike, after all these months spent together you will have enough stories to tell for the next years; Nuria, with hindsight I would have wanted you sitting next to me, you know; Paul, I will give you my recipe for the pasta coi broccoli one day; Awse, continue to keep up the name of Mauro in MC2, only you can do it; Napo, the fernet branca you gave me is still in my Swedish fridge, and I guess it will stay there for a while; Alessia, one day I will finish to listen to your 10 mins audio messages.

I found friends in you, thank you.

To Edo erotic "The unemployed". Thank you for everything, you helped me a lot both inside and outside the cleanroom. You also made me realize how expensive the systembolaget is. We had great time together and I hope it was just the beginning. Maraina, peanut and you are the best!

To the "Bokachoda", Arpita. You are so nice and all the adventures we went through were amazing. Edo, you, and me were a so magic trio. I'll miss both of you.

To Riccardo Arpaia, my co-supervisor for both Chalmers and Politecnico di Milano. You are the person that I have to thank the most. I don't even know where to start. There are a lot of great scientist out there, but finding someone that is also a great person is very rare, and you are one of them. You are an inspirational model to me. Thank you for all the help and the support you gave me, for all the patience you had in putting up with Andrea and me, for all the inspiring discussion we had about science, and also for all the interesting discussion we had, not about science. I will never thank you (and Flavia) enough, next time I'll keep Lorenzo busy for an entire day to let you rest a little!

Finally, I want to thank all my family, and my girlfriend Camilla (un bicchierino), for all the support and love that made me arrive where I'm now. Grazie di cuore!

Mmmm... Maybe I'm forgetting someone... Oh yes, Andrea!

Andrea, what to say... Sorry if I'm not writing a chapter to thank you, I wanted to but these acknowledgments are already quite long. We took the plane from Pisa together to start this adventure. We did to many things together that it will be strange to not have you around everyday. It has been really a pleasure to share this experience with you, and it will be even better to have a dinner on you at Noma in Copenhagen. This is just a goodbye, see you soon!

List of Acronyms

Below is the list of acronyms that have been used throughout this thesis listed in alphabetical order:

AF	Antiferromagnetic
AFM	Atomic force microscopy
ARPES	Angle resolved photoemission spectroscopy
LBCO	$\text{La}_{2-x}\text{Ba}_x\text{CuO}_4$
BSCCO	$\text{Bi}_2\text{Sr}_2\text{CaCu}_2\text{O}_{8+x}$
CDF	Charge density fluctuations
CDW	Charge density wave
FWHM	Full width half maximum
GL	Ginzburg-Landau
HTS	High critical temperature superconductor
IVC	Current voltage characteristic
LBCO	$\text{La}_{2-x}\text{Ba}_x\text{CuO}_4$
LN2	Liquid nitrogen
LSAO	LaSrAlO_4
LSCO	$\text{La}_{2-x}\text{Sr}_x\text{CuO}_4$
MBE	Molecular beam epitaxy
PDW	Pair density wave
PLD	Pulsed laser deposition
PPMS	Physical property measurement system
RHEED	Reflection high energy electron diffraction
SDW	Spin density wave
SEM	Scanning electron microscopy
STO	SrTiO_3
XRD	X-ray diffraction
XRR	X-ray reflectivity
YBCO	$\text{YBa}_2\text{Cu}_3\text{O}_{7-\delta}$

list of symbols

Below is the nomenclature of indices, sets, parameters, and variables that have been used throughout this thesis.

Indices

A	Magnetic vector potential
B	Magnetic field
E	Electric field
δ	Oxygen non-stoichiometry
Δ	Superconducting gap
d_{T-s}	target to substrate distance
e	Electronic elementary charge
e^*	Effective electron charge
F	Free energy
F_n	Free energy of the normal phase
\hbar	Reduced Plank constant
i	Imaginary unit
I_c	Critical current
J_d	Depairing current density
J_s	Superconducting current density
J_v	Vortex entry critical current density
λ_L	London penetration depth
l	Nanowire length
m	Mass
μ_0	Vacuum permeability
n_s	Superfluid density

p	Doping parameter
ϕ	Phase
Φ_0	Flux quantum
Ψ	Order parameter
R_{Au}	Gold resistance
R_{nw}	Nanowire resistance
t	Thickness
T_c	Critical temperature
T_c^0	Zero resistance critical temperature
T_c^{on}	Onset critical temperature
T_c^{mid}	Midpoint critical temperature
v_s	Superfluid velocity
w	Nanowire width
ξ	Coherence length

Contents

List of Acronyms	ix
Nomenclature	xi
List of Figures	xv
List of Tables	xix
1 Background of superconductivity	5
1.1 From mercury to cuprates	5
1.2 Depairing current density in nanowires	7
2 The cuprates	9
2.1 High critical temperature superconductivity	9
2.2 $\text{La}_{2-x}\text{Sr}_x\text{CuO}_4$	11
2.2.1 Crystal structure and doping mechanism	12
2.2.2 Phase diagram	13
2.2.2.1 Strange metal	14
2.2.2.2 Pseudogap	15
2.2.2.3 Charge and spin order	17
3 Growth and characterization of LSCO ultra-thin films	21
3.1 Growth of LSCO	21
3.2 Choice of the substrate: LaSrAlO_4	24
3.2.1 Substrate treatment and characterization	25
3.3 Pulsed Laser Deposition assisted by RHEED	26
3.4 LSCO film characterization	28
3.4.1 RHEED	29
3.4.2 Surface	30
3.4.3 Crystallinity	31
3.4.4 Electric transport	34
3.4.5 Ozone post-annealing	36
4 Nanowires fabrication	39
4.1 Fabrication steps	39

5	Nanowires measurements	43
5.1	Nanowire geometry and film used for the nanopatterning	43
5.2	Measurement setup	45
5.3	Results	45
5.3.1	Resistivity vs temperature	46
5.3.2	Current-voltage characteristics	48
5.3.3	Temperature dependence of the critical current density	49
6	Summary and outlook	53
A	Appendix 1	I
A.0.0.1	LSCO nanowires	I

List of Figures

2.1	Unit cell of some typical cuprates with different structure and number of copper oxide planes per unit cell. The CuO_2 planes are highlighted in blue. (a) $\text{La}_{2-x}\text{Sr}_x\text{CuO}_4$, (b) $\text{YBa}_2\text{Cu}_3\text{O}_7$, (c), (d) . Adapted from reference [1].	10
2.2	superconducting energy gap symmetry on a circular Fermi surface for: (a) s-wave order parameter and (b) $d_{x^2-y^2}$ order parameter. Red + represent positive phase sign while blue - represent negative phase sign. from ref. [2].	11
2.3	a) Crystal structure of the undoped LSCO: La_2CuO_4 . b) Hole doping mechanism by metal cation substitution and intercalation of interstitial oxygen. The stacking sequence of both compounds is shown, where the CuO_2 planes is highlighted in blue. Adapted from reference [1]	12
2.4	Temperature vs doping phase diagram of LSCO. The violet area is the antiferromagnetic order (AF) below the Néel temperature T_N , the pink area is the pseudogap phase below T^* , the yellow area is the charge density wave (CDW) precursor order, the orange one is the spin density wave (SDW) order below T_{SDW} , in red there is the stripe order region, and finally in green there is the superconducting phase below the transition temperature T_c . Adapted from ref. [3–5].	14
2.5	Schematic Fermi surface of the cuprates: (a) in the strange metal phase at room temperature, (b) Fermi arcs in the pseudogap phase below T^* . From ref. [2].	16
2.6	Picture of the stripe order in LSCO in CuO_2 planes seen from above. The antiferromagnetic Mott-like regions, where the spins are indicated by blue arrows, are separated by narrow rivers of mobile charge (purple circles). Adapted from [6].	17
2.7	Simplified illustration of the incommensurate CDW in LSCO superimposed to one of the orientation of the CuO_2 planes seen from the side. The green and blue circles are Cu and O atoms respectively. $\delta\rho$ is the charge density deviation from the average value, a is the lattice parameter, and λ_{CDW} the wavelength of the CDW modulation.	18

3.1	T_c of thin film of LSCO grown on two different substrates (STO and LSAO) subject to tensile and compressive strain, compared to the bulk T_c values. Red circles are T_c of films grown on LSAO, while the blue circles are T_c of films grown on STO from reference [7]. The dotted line represent the T_c of the bulk compound, from [8].	22
3.2	Oxygen and strontium co-doping effect on LSCO films. Adapted from reference [8, 9]	23
3.3	Quick illustration of the difference in in-plane lattice parameter of the substrates LSAO and STO compared to LSCO, with consequent type of strain induced.	24
3.4	AFM image of the S06 LSAO substrate surface: a) before any treatment, b) after annealing for 3 h at 950 C.	26
3.5	RHEED diffraction pattern of one of the SurfaceNet LSAO substrate. The strong specular spot, and the streak-like side spots indicate a flat surface.	26
3.6	Scheme of the pulsed laser deposition system and the RHEED system used to monitor the growth.	27
3.7	Schematics of different types of surface, in real-space morphology, in reciprocal space, and their RHEED pattern. Adapted from reference [10].	28
3.8	a) RHEED pattern of one LSCO film after the deposition. b) Intensity as a function of time of the central spot of the RHEED pattern during the growth. The signal is magnified in the inset to highlight the surface relaxation characteristic of the layer-by-layer and step flow growth mode.	29
3.9	AFM image of the surface of one of the films after the deposition. Despite the presence of precipitates (indicated by the arrow) on the film, the surface is flat with a low roughness value R_q . The image was taken in tapping mode.	30
3.10	X-ray reflectivity measurement of one representative LSCO film. The scan is centered at the critical angle of the surface. The blue line represent the experimental data of the XRR profile of the film, the red line is the fitted curve. The estimated thickness of the film is shown in the box.	31
3.11	a) $2\theta - \omega$ symmetric scan of the LSCO (004) and LSAO (004) reflections. It is possible to note the presence of a smaller extra peak, corresponding to the La_2O_3 (011) reflection. b) Rocking curve of the LSCO (006) reflection. The FWHM of the peak is reported on the top right part of the plot.	32
3.12	$2\theta - \omega$ symmetric scan of the LSCO (00n) and LSAO (00n) reflections in the range 10° - 80° . The smaller reflection peak belong to LSCO, while the higher in intensity to LSAO. The out-of-plane c parameter estimated from the brag peak position of LSCO (is reported in the top right part of the plot.	33

3.13	In-plane $R(T)$ normalized at 45 K, and $dR(T)/dT$ around the superconducting transition for one of the best obtained film. The onset of the transition, defined as the 10% of the first derivative is reported in green. In purple the midpoint of the transition, defined as the maximum of the first derivative. In red the T_c^0 , defined as the temperature at which the resistance completely vanish. The width of the transition is reported in gray, defined as the FWHM of the first derivative.	34
3.14	Histogram for T_c of our superconducting LSCO films.	35
3.15	Histogram for T_c of optimally doped LSCO film grown by MBE with thicknesses between 50 and 5000 Å on LSAO cleaned a) by organic solvent and b) by chemical etching with methanol solutions of 1 vol.% hydrochloric acid (HCl). From reference [11].	36
3.16	Effect of the ozone post-annealing on two samples. The orange line is one sample representative for the "low T_c " films before the post-annealing in ozone, while the yellow line is the same sample after the post-annealing. The blue and light-blue lines belong to the best sample with highest T_c before and after the post-annealing in ozone. The $R(T)$ are normalized on the $R(T = 300 \text{ K})$ value for an easier comparison of the results.	36
4.1	Schematics of the fabrication steps for LSCO nanowires described in the text. Adapted from reference [12].	40
5.1	Resistance vs temperature measurement of the 50 nm thick film we used for the nanopatterning.	44
5.2	Scanning Electron Microscopy image of a 200 nm wide nanowire after the lift-off (step 6 in chapter 4). In order to avoid current crowding effect the angles of the nanowire are rounded.	44
5.3	Schematics of the 4K dip-stick setup.	45
5.4	Resistance around the superconducting transition for a 50 and 500 nm width nanowire. It can be noticed that the the transition is broadened in both cases, but it is more pronounced in the narrowest nanowire.	46
5.5	Current voltage characteristics for a 50 nm width wire, in blue, and a 500 nm width wire, in red.	48
5.6	temperature dependence of the critical current density for a 50 nm width nanowire. The data are fitted with the Bardeen expression.	49
5.7	Normalized critical current density as a function of temperature for a) overetched and optimally etched YBCO nanowires, b) YBCO nanowires with a gold capping layers. From ref. [13].	50

List of Tables

2.1	Values of upper critical field, London penetration depth, and coherence length for optimally doped LSCO, YBCO, and BSCCO. The value for the critical field is out-of-plane, typically used in experiments, while the values for λ and ξ are in-plane, where conduction take place. These values are only indicative. From ref [14–20].	10
A.1	Ar ⁺ ion milling parameters.	II

Introduction

Soon after the discovery of high critical temperature superconductivity in the copper oxide (cuprate) $\text{La}_{2-x}\text{Ba}_x\text{CuO}_4$ (LBCO) in 1986 [21], it became clear that the standard quantum theory of the electronic properties of solid, successfully describing normal metals and conventional superconductors, entirely fails to account for the peculiar properties of this new class of compounds. Cuprates are characterized by a quasi-two-dimensional layered structure, containing one or more weakly coupled copper dioxide (CuO_2) planes, that dominates the physics of these materials, interleaved by spacer layers. The CuO_2 planes can be electron- or hole-doped by intercalation of oxygen and/or chemical substitution of metal cations in the spacer layers, that act as charge reservoirs. The quasi-2D character of the copper oxide planes implies a weak screening of the Coulomb interaction and thus strong electron-electron correlations [22], drastically enhancing quantum effects. This, together with the possibility to tune the doping level in the CuO_2 planes give rise to a plethora of phases and nanoscale orders, well summarized in the temperature-doping (T - p) phase diagram. The understanding of this class of materials is puzzling not only in the superconducting state, but also in the fascinating normal state from which superconductivity arises. The normal state is indeed pervaded by the spontaneous emergence of various phases and ordered states, tuned by the doping and driven by many competing degrees of freedom. At high temperature the normal state of cuprates is characterized by the *strange metal* phase, whose most striking characteristic is the linear temperature dependence of the resistivity. Lowering the temperature below a characteristic temperature T^* , the *pseudogap phase* takes over, characterized by the opening of a gap in the Fermi surface. Moreover, in strongly correlated systems as the cuprates, the tendency of the valence electrons to segregate in periodically modulated features can lead to the formation of exotic charge and spin orders. In particular, charge density modulations, in the form of long-ranged charge density waves (CDW) and short-ranged charge density fluctuations (CDF), related to translational and rotational symmetry breaking, are ubiquitous in all cuprate families [23, 24]. These modulations lay along the a - and b -axis of the copper oxide planes and are incommensurate with respect to the the lattice constants. They have been confirmed by neutron scattering [25], scanning tunnel microscopy [26], and resonant elastic/inelastic x-ray scattering experiments [27]. CDW, mostly present in the underdoped region of the phase diagram, are in competition with superconductivity as demonstrated by their intensity, being maximum at a doping level ($p \sim 0.12$) where the superconducting critical temperature is depressed [23, 27]. On the other hand, CDF pervade a large portion of the phase diagram (both in temperature and doping) surviving also above the pseudogap temperature T^* . For their characteristic they have been

connected to the strange metal phase. In addition to charge modulations, at low doping also another type of electronic order is present, the spin density wave (SDW) [28], that is a periodic modulation of the electronic spin density. Indeed, in every parent compound (at zero doping level) of a cuprate family, each copper site has a single unpaired electron. Due to the Coulomb interaction, the electrons are strongly localized, while to minimize the energy of the spin interaction electrons order in an antiferromagnetic fashion. Such compound is called Mott insulator [29]. In all the hole-doped cuprates, increasing the doping level lead to the disappearance of the commensurate antiferromagnetic order, that is replaced by an incommensurate spin order (the SDW). Whether on one side the CDW and SDW orders are a common feature to all cuprates, in the La-based cuprates there is also a region of the phase diagram where the charge and spin modulations are locked by a well defined relation of periodicity, forming the so-called stripe order [30]. Such stripes are likely to occur most strongly at the doping level $p \sim 0.12$. The spin part of the stripe orders antiferromagnetically and resembles a narrow ribbon of Mott insulator, while the charge carriers are confined in lattice-constant wide lines (called "rivers" of charge) interspersing the AF regions by a period of four lattice unit cells.

The way these quantum electronic orders are intertwined, and are eventually responsible for the phenomenology in HTS compound, is still not clear. There are several theoretical models in which the collective charge density fluctuations are considered pivotal to explain the anomalous properties of both the normal and the superconductive state [31–33]. Unravelling this complex picture is an undertaking challenge, and new experiments, to tackle the problem from new perspectives, are continuously required. Whereas the characteristic lengthscale of these entwined orders, together with the London penetration depth and the coherence length, is in the order of the nanometers, one possible way to shed light on their nature is the experimental investigation of structure at the nanoscale. The confinement induced by structures of reduced dimensionality and the strain induced by the substrate are two extremely powerful knobs to manipulate these nanoscale orders and figure out their mutual interaction. Indeed, recently it has been demonstrated that in $\text{YBa}_2\text{Cu}_3\text{O}_{7-\delta}$ (YBCO) nanostructures of the order of the CDW correlation length, the phase diagram can be modified by the strain induced by the substrate, suppressing the CDW and restoring the strange metal phase [2]. This finding add an important dowel to the puzzle, but the global picture is still incomplete. Therefore, there is a great interest in the investigation of other cuprate families, such as the La-based one where the stripes are present. In particular, $\text{La}_{2-x}\text{Sr}_x\text{CuO}_4$ (LSCO) is considered the prototype of cuprates, for its rather simple crystal structure and the presence of only one copper oxide plane per unit cell. Moreover, in LSCO thin films the superconductive state is strictly related to the strain induced by the substrate, even more than in other cuprates. Indeed, it is well know that in LSCO compressive in-plane strain can drastically enhance the critical temperature [34], while tensile in-plane strain reduce it [7]. However, growing LSCO in thin film form is not straightforward, and fabricating LSCO nanostructure is even more complicated. Indeed, to our knowledge there is only one previous work on LSCO nanorings [35], and one on LSCO nanowires [36]. In the latter work the results do not reconcile with the Ginzburg-Landau theoretical model, and the nanowire lateral dimension is

still larger than 200 nm.

In this large framework, this thesis focus on the film growth optimization and nanopatterning of optimally doped LSCO, laying the basis for future studies of the ground state of this compound when affected by the strain induced by the substrate. In Chapter 1 a brief overview of the theoretical background of superconductivity is given, with a focus on the physics of the nanowires relevant for the discussion of the experiments, while in Chapter 2 the properties of the cuprates, in particular of LSCO, are introduced.

Then, the two main parts of this work are presented:

In the first part (Chapter 3), the results of the LSCO ultra-thin film (15 u.c.) growth optimization by Pulsed Laser Deposition (PLD) are presented. At the beginning of the chapter we give an overview on the previous results about the growth of LSCO, with reference to the current literature on the subject, in order to understand the significance of the results that will be mentioned. The films were characterized in term of surface with the Reflection High Energy Electron diffraction (RHEED) and Atomic Force Microscopy (AFM), in terms of crystallinity with X-ray Diffraction (XRD) and X-ray Reflectivity (XRR), and in terms of transport properties with a Physical Properties Measurements System (PPMS).

The second part of the thesis consists of the nanofabrication of nanowires and the evaluation of their quality. In Chapter 4 we present the main steps of the nanofabrication process, already successfully used for other cuprates. Its detailed description is reported in appendix ???. The key feature of our improved nanofabrication process is the presence of a gold capping layer between the film and the carbon hard mask. This layer protect the nanostructures during the fabrication process, in particular it prevents them to be overheated during the etching step, and it protects them during the oxygen plasma etching step. This allowed us to obtain nanowires, with the superconducting properties of the pristine material, down to 50 nm width. In Chapter 5 we present the results of the measurements of the nanowires. It is worth noting that there are no previous work to compare our results with, therefore we interpreted and discussed our results with reference to YBCO state-of-the-art nanowires. We measured the resistance temperature dependence of the 50 and 500 nm width nanowires, finding a broadening of the transition for the narrowest nanowires due to thermal fluctuations. Then, we measured the current-voltage characteristic (IVC), to determine the values for the critical current density. Finally, we have measured the temperature dependence of the critical current density for a 50 nm width nanowire, fitting the data with the Bardeen expression. We show how it is possible to use the extracted value of the critical current density at zero temperature as an indication of the quality of the nanowires, comparing that value with the theoretical limit for the depairing current density, due to vortex entry, predicted by the Ginzburg-Landau model. Moreover, comparing the results with YBCO nanowires, we show how the trend of the critical current temperature dependence is another useful indication of the quality of the nanowires.

Finally, in Chapter 6 we will draw the conclusion and we will give an outlook for the next steps to take in this project to improve the results obtained in this thesis, and to investigate the ground state of LSCO at the nanoscale.

1

Background of superconductivity

In this chapter the main results on superconductivity are presented to provide the necessary theoretical background for the understanding of the thesis.

1.1 From mercury to cuprates

Superconductivity was discovered in Leiden in 1911 by Kamerling Onnes [37] while he was trying to test the Drude model at the lowest possible temperature. During the measurement of the electrical resistance of mercury, he noticed that, below a certain temperature, now called critical temperature, $T_c = 4.2$ K, the resistance abruptly vanished within a small temperature interval. This was the first hallmark of what would have been called superconductivity, and one of the property characterizing superconductors: the perfect conductivity. The discovery was so unbelievable that Onnes required some time to realize that it was not a mere failure of the instrumentation. With his discovery, Onnes opened a new era in solid state physics.

In 1933 the German physicists W. Meissner and R. Ochsenfeld [38], discovered the second property characterizing superconductivity, the Meissner-Ochsenfeld effect, i. e. the expulsion of the magnetic field, lower than a critical field B_c , by a superconductor when cooled below T_c .

Few years later, another step in the understanding of superconductivity was done. The physicists F. and H. London [39] proposed the following two equations to describe the electrodynamics of superconductors.

$$\frac{\partial J_s}{\partial t} = \frac{n_s e^{*2}}{m^*} E \quad (1.1)$$

$$\nabla \times J_s = \frac{n_s e^{*2}}{m^*} B \quad (1.2)$$

where J_s is the superconducting current density, E and B are the electric and magnetic field inside the superconductor, n_s is the density of superconducting electrons that flow without dissipation, e^* and m^* are respectively the effective charge and mass of the superconducting electrons. The London equations describe the aforementioned characteristic properties of superconductors.

The first equation (1.1) describes the perfect conductivity: a finite electric field accelerates the superconducting electrons, and a supercurrent density J_s can be sustained without dissipation and in absence of an electric field. The second equation

1. Background of superconductivity

(1.2), when combined with the Ampère's law $\nabla \times B = \mu_0 J$, where μ_0 is the vacuum permeability, describes the Meissner-Ochsenfeld effect:

$$\nabla^2 B = \frac{1}{\lambda_L^2} B, \quad \lambda_L = \sqrt{\frac{m^*}{\mu_0 n_s e^{*2}}} \quad (1.3)$$

The solution of equation 1.3 gives an exponentially decaying magnetic field at the surface of a superconductor, i.e. the magnetic field is screened from the bulk of the superconductor. The screening length is the so called *London penetration depth*. Although the London equation represents an important milestone in the understanding of superconductivity, they fail to describe the property of a superconductor in presence of a strong magnetic field close to the critical field B_c , for which the superconducting state is destroyed, or when the superfluid density n_s is not constant in space.

In 1950, The Russian physicists L. Landau and V. Ginzburg [40] extended the London model, postulating a phenomenological model based on the Landau's theory of second-order phase transitions. The theory is valid for temperature close to the critical temperature T_c of a superconductor and considering the superfluid density as a function of space $n_s(r)$. They introduced a complex order parameter (slowly varying in space near T_c) defined as

$$\Psi(r) = |\Psi(r)| e^{i\phi r} \quad (1.4)$$

where $|\Psi(r)| = \sqrt{n_s(r)}$ and $\phi(r)$ are respectively the amplitude and the phase as a function of position. The free energy of the superconducting system $F = F(\Psi, T)$, in presence of an external magnetic field B , can be expanded in series of Ψ and $\nabla\Psi$, taking the form:

$$F = F_n + \alpha |\Psi|^2 + \frac{\beta}{2} |\Psi|^4 + \frac{1}{2m^*} |(-i\hbar\nabla - e^*A)\Psi|^2 + \frac{B}{2\mu_0} \quad (1.5)$$

where F_n is the free energy of the normal phase, $\alpha = \partial F / \partial n_s$ and $\beta = \partial^2 F / \partial n_s^2$ are temperature dependent parameter, and A is the magnetic vector potential. The condition for the minimum free energy state is found by integrating over the system volume and minimizing eq. 1.5 with respect to $\Psi(r)$ and $\Psi^*(r)$. The results are the two Ginzburg-Landau equations:

$$\alpha |\Psi| + \beta |\Psi|^2 \Psi + \frac{1}{2m^*} (-i\hbar\nabla - e^*A)^2 \Psi = 0 \quad (1.6)$$

$$J_s = \frac{\hbar e^*}{2im^*} (\Psi^* \nabla \Psi - \Psi \nabla \Psi^*) - \frac{e^{*2}}{m^*} A |\Psi|^2 \quad (1.7)$$

Moreover, the Ginzburg-Landau theory introduces a new length scale, the *coherence length* ξ . The relation between ξ and Ψ , in absence of an external magnetic field and when Ψ is small, can be expressed in a similar form to equation 1.3:

$$\nabla^2 \Psi = \frac{1}{\xi^2} \Psi, \quad \xi = \sqrt{\frac{\hbar^2}{2m|\alpha|}} \quad (1.8)$$

where α is a material dependent constant. ξ can be thought as the length scale representing the spatial variation of the order parameter. The ratio $k = \frac{\lambda_L}{\xi}$ is the Ginzburg-Landau parameter, and one can divide superconductors in two large families (type I and type II) depending on the value of this ratio, according to how the superconductivity interacts with the magnetic field. In type I superconductors ($k < \frac{1}{\sqrt{2}}$) the magnetic field is expelled from the bulk up to $B = B_c$, after which the superconducting state is destroyed. In type II superconductors ($k > \frac{1}{\sqrt{2}}$), there are instead two critical fields $B_{c,1}$ and $B_{c,2}$. For $B < B_{c,1}$ the field is expelled as in type I superconductors, this is the so-called Meissner state. For $B_{c,1} < B < B_{c,2}$ is more energetically favourable for the field to penetrate into the superconductor in an ordered lattice of flux lines, where the magnetic flux in each line is the magnetic flux quantum $\phi_0 = \frac{h}{2e}$. This is the so-called Abrikosov state, named after A. A. Abrikosov, who, in 1957, described the behaviour of type II superconductors [41]. It is worth noting that $B_c \ll B_{c,2}$, making type II superconductors suitable for high magnetic field applications. Although, the Ginzburg-Landau model was very successful in describing the property of superconductors, the microscopic mechanism underlying superconductivity was still unknown.

In 1957, the American physicists J. Bardeen, L. Cooper, and J. R. Schrieffer proposed the first microscopic theory of superconductivity [42], the BCS theory. According to their model, for $T < T_c$, electrons of opposite spin and momentum near the Fermi surface can form a bound state due to a weak attractive potential mediated by the electron-phonon interaction, as suggested by the isotope effect observed in 1950 by Maxwell [43], creating the so-called *Cooper pair*. Here, the coherence length ξ is the length scale of the interaction and the energy required to break a Cooper pair corresponds to 2Δ , where Δ is the energy gap in the excitation spectra of the superconductor. The BCS theory was experimentally confirmed in the following years and Bardeen, Cooper, and Schrieffer were awarded with the Nobel prize in 1972.

However, about 35 years after its formulation, the BCS theory was challenged by the discovery of a new class of superconductors. These compounds are the cuprates, characterized by the presence of copper-dioxide planes, and with critical temperature up to 138 K at ambient pressure. After decades of intensive studies, the microscopic mechanism underlying the unique properties of cuprates is not fully understood yet, making superconductivity in these compounds one of the biggest mystery of solid state physics nowadays. In chapter 2, the main features and characteristics of the cuprates will be summarised.

1.2 Depairing current density in nanowires

In order to better understand the results in chapter 5 and their significance, the Ginzburg-Landau model in the case of superconducting narrow nanobridge with thickness t , width w , and length l , should be reviewed. From the GL equations (eq. 1.6 and eq. 1.7) it is possible to derive the depairing current density J_d , above which the order parameter (pair density) is locally suppressed due to the nucleation of phase slips centers i.e. phase difference changes between two superconducting

region by 2π in a short time.

In the limit of long ($l \gg \xi$) and one-dimensional ($w, t \ll \lambda^2$ and $wt \ll \lambda^2$) bridge the free energy can be written as [44]:

$$F = F_n + \alpha|\Psi|^2 + \frac{\beta}{2}|\Psi|^4 + |\Psi|^2 \frac{1}{2}m^*v_s^2 \quad (1.9)$$

where v_s is the superfluid velocity, defined from the relation $J_s = e^*|\Psi|^2v_s$. The condition $w, t \ll \xi$ ensure that the order parameter $\Psi(r)$ is constant across the cross section of the bridge, while the condition $wt \ll \lambda^2$ ensure that the uniform current density and the kinetic energy of the superconducting carrier dominates over the magnetic self-field term produced by the same current, that can therefore neglected in eq. 1.5. The order parameter inside the nanowire (NW) can be defined as:

$$\Psi^{NW}(x) = |\Psi^{NW}|e^{ix\phi/l} \quad (1.10)$$

Minimizing eq. 1.9 the modulus of the wave function can be found:

$$|\Psi^{NW}|^2 = |\Psi_\infty^{NW}|^2[1 - (\frac{\xi}{l})^2\phi^2] \quad (1.11)$$

where $|\Psi_\infty^{NW}|^2$ is the modulus of the wave function at zero phase difference. The current-phase relation for a long one-dimensional nanowire can be determined by substituting eq. 1.10 and eq. 1.11 in eq. 1.7, obtaining:

$$J_s^{NW} = \frac{\Phi_0}{2\pi\mu_0\lambda^2\xi}[(\frac{\xi}{l})\phi - (\frac{\xi}{l})^3\phi^3] \quad (1.12)$$

Finally, maximizing the previous equation with respect to ϕ/l , it is possible to determine the maximum value of ϕ_d , corresponding to the depairing current density J_d defined as:

$$J_d = \frac{\phi_0}{3\sqrt{3}\pi\mu_0\lambda^2\xi} \quad (1.13)$$

It is worth noting that we have derived this expression in the limit of long one-dimensional nanowire. For bridges wider than $w > 4.44\xi$ a different regime has to be considered, due to the coherent motion of Abrikosov vortices inside the structure. However, for bridge thicknesses lower than $t < \lambda$ and widths lower than $w < \lambda_P$, with $\lambda_P = \lambda^2/t$ the Pearl length, the current can be considered homogeneous, allowing to reduce the GL equations to the one-dimensional form [45], with the only difference that the maximum critical current density is not given by depairing effect, i.e. phase slips, but by Abrikosov vortices overcoming the bridge edge barrier. As suggested by Bulaevskii et al. [46], in this case the value of the critical current density due to vortex entry J_v is smaller than the depairing current for the 1D case

$$J_v = 0.826J_d \quad (1.14)$$

In real nanostructure it is possible to approach this value only in case of very high homogeneity of the wire. Therefore, the critical current density value of real nanowires, compared to the theoretical limit, can be used as an effective indication of the quality of the nanowire.

2

The cuprates

Cuprate high-critical temperature superconductors (HTS) are a family of superconductors, characterized by a layered structure containing one or more weakly coupled copper-dioxide (CuO_2) planes per unit cell, alternated by spacer layers. The parent material is an Mott insulator, but when it is doped, either with electrons or holes, a wealth of phenomena emerges. In this chapter, the most important features of cuprates are presented, with a particular focus on LSCO, the HTS material which is object of this thesis work.

2.1 High critical temperature superconductivity

Cuprate HTS were discovered in 1986 by Bednorz and Müller, who observed a $T_c \approx 35$ K in hole-doped Ba-La-Cu-O system [21]. This discovery was embraced with great enthusiasm by the scientific community, and few months later several other HTSs were discovered. At first $\text{La}_{2-x}\text{Sr}_x\text{CuO}_4$ (LSCO), having the same La-based K_2NiF_4 -type structure but with a slightly higher $T_c = 39$ K [47], subsequently $\text{YBa}_2\text{Cu}_3\text{O}_{7-\delta}$ (YBCO) with a $T_c = 92$ K [48], the first cuprate with T_c above the boiling point of nitrogen, that opened a completely new scenario for superconductors applications.

In the following years many other HTS materials were discovered, both electron- and hole-doped, with T_c up to 138 K at ambient pressure in mercury compounds [49, 50]. Nowadays, LSCO together with YBCO and $\text{Bi}_2\text{Sr}_2\text{CaCu}_2\text{O}_{8+x}$ (BSCCO) are the most studied HTS both for fundamental research and applications.

In figure 2.1 the structure of different cuprates is reported. The common element among cuprates is their quasi-two-dimensional layered structure, containing one or more CuO_2 planes per unit cell (see figure 2.1), separated by spacer layers, generally containing metal cations and/or oxygen atoms. The CuO_2 planes can be doped by introducing extra electrons or holes. The dopants (that can be excess oxygen atoms or substitutional metal cations), are introduced in the spacer layers, and act as charge reservoir. Depending on the type of dopant, the electrons are either transferred from the CuO_2 planes to the charge reservoirs (hole doping), or viceversa (electron doping). For example, in LSCO, the material object of this thesis, hole-doping is achieved by random chemical substitution of metal cations with higher valence. In contrast, in YBCO hole-doping is achieved by introducing excess oxygen, that accommodate along the [010] direction (see figure 2.1 (b)) giving rise to CuO chains in the top and bottom planes. In any case, the carriers are usually sharply localized in the CuO_2 planes, making the coupling between these planes very weak.

2. The cuprates

For this reason, cuprates often have extremely anisotropic properties, both in the normal and superconducting state, when measured in- or out-of-plane.

Cuprates are type II superconductors ($\xi \ll \lambda$), and $B_{c,2}$ is in the order of 50-100 T (see table 2.1 for a comparison of the most common cuprates). Unlike conventional superconductors (i.e. superconductors described by the BCS theory or its extensions), that present an isotropic superconducting energy gap in momentum space (s-wave order parameter), cuprates have a strongly anisotropic energy gap symmetry.

Material	$B_{c,2}$ [T]	λ [nm]	ξ [nm]
$\text{La}_{1.85}\text{Sr}_{0.15}\text{CuO}_4$	80	300	3
$\text{YBa}_2\text{Cu}_3\text{O}_7$	130	135	1.6
$\text{Bi}_2\text{Sr}_2\text{CaCu}_2\text{O}_8$	32	300	3

Table 2.1: Values of upper critical field, London penetration depth, and coherence length for optimally doped LSCO, YBCO, and BSCCO. The value for the critical field is out-of-plane, typically used in experiments, while the values for λ and ξ are in-plane, where conduction take place. These values are only indicative. From ref [14–20].

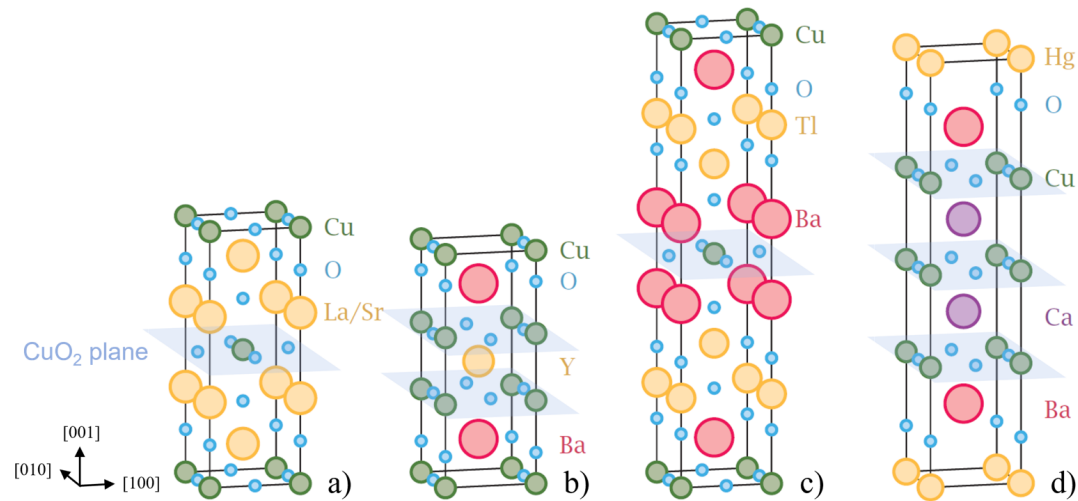


Figure 2.1: Unit cell of some typical cuprates with different structure and number of copper oxide planes per unit cell. The CuO_2 planes are highlighted in blue. (a) $\text{La}_{2-x}\text{Sr}_x\text{CuO}_4$, (b) $\text{YBa}_2\text{Cu}_3\text{O}_7$, (c), (d). Adapted from reference [1].

Transport [51] and angle-resolved photoemission spectroscopy experiments [52] have shown that, in cuprates, the symmetry of the gap varies in k -space according to $\Delta(\vec{k}) = \Delta_0(\cos(k_x a) - \cos(k_y a))$ [51], thus the gap has predominant $d_{x^2-y^2}$ orbital character, i.e. is maximum along the Cu-O bonds and has nodes along the diagonals (see fig.2.2).

The two-dimensional character of the CuO_2 planes, together with the low carrier density, result in strong electron-electron interactions [22], that give rise to a rich and complex electronic phase diagram, where the different phases and nanoscale orders are well summarised as function of the temperature and of the doping. Indeed, an undoped cuprate is "naturally" an antiferromagnetic insulator, but introducing holes into the CuO_2 planes, the material become first superconducting, and then a normal metal. In addition, overlapped to these phases there are also more exotic electronic orders that will be described in the next section.

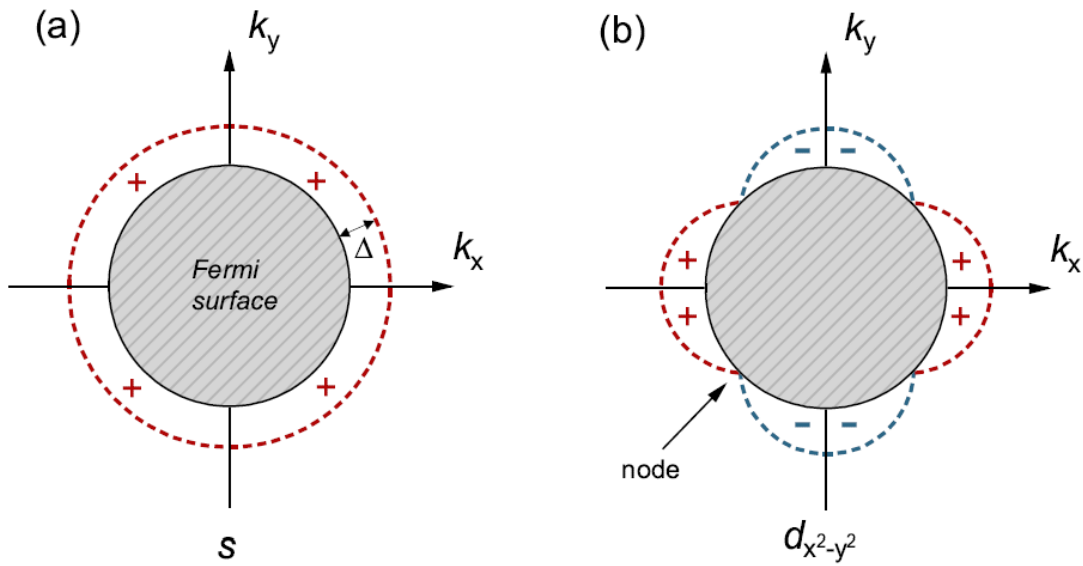


Figure 2.2: superconducting energy gap symmetry on a circular Fermi surface for: (a) s-wave order parameter and (b) $d_{x^2-y^2}$ order parameter. Red + represent positive phase sign while blue - represent negative phase sign. from ref. [2].

2.2 $\text{La}_{2-x}\text{Sr}_x\text{CuO}_4$

$\text{La}_{2-x}\text{Sr}_x\text{CuO}_4$ is one of the most studied cuprate. It is regarded as the prototype of a cuprate because of the rather simple crystal structure, the presence of only one CuO_2 plane per unit cell, and the possibility to control the doping easily by changing the strontium concentration. These features makes LSCO a model system to investigate the properties of the superconductive and normal state of cuprates.

2.2.1 Crystal structure and doping mechanism

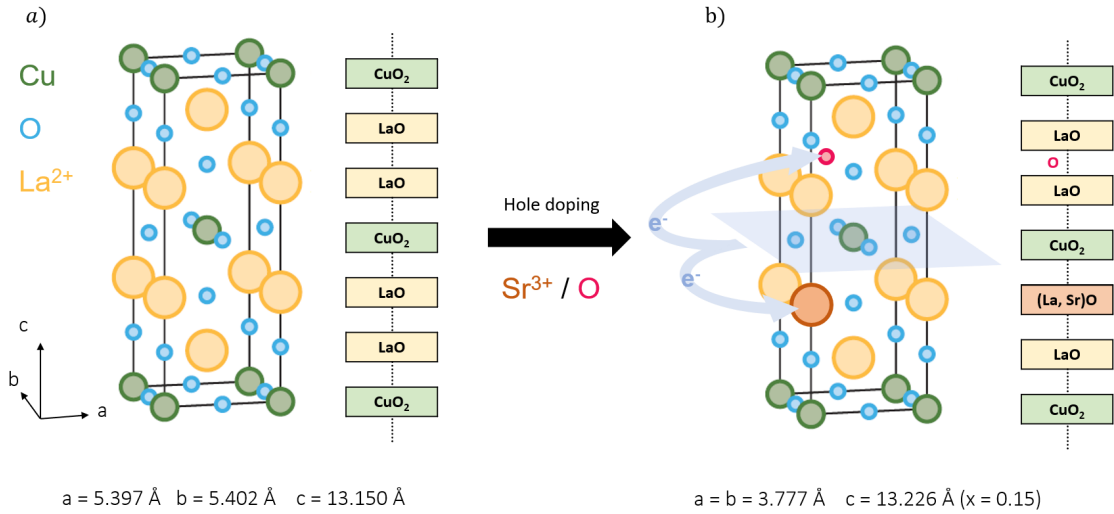


Figure 2.3: a) Crystal structure of the undoped LSCO: La_2CuO_4 . b) Hole doping mechanism by metal cation substitution and intercalation of interstitial oxygen. The stacking sequence of both compounds is shown, where the CuO_2 planes is highlighted in blue. Adapted from reference [1]

$\text{La}_{2-x}\text{Sr}_x\text{CuO}_4$ crystallize in a tetragonal layered K_2NiF_4 structure with lattice constant $a = b = 3.777 \text{ \AA}$ and $c = 13.226 \text{ \AA}$ for $x = 0.15$ [53]. The structure contains oxygen in octahedral coordination around Cu atoms, while the La/Sr atoms are surrounded by nine oxygen. It is worth noting that LSCO is regarded as a single CuO_2 plane cuprate, even if from the unit cell structure there are seemingly two planes, with the top and bottom planes shared with neighbouring cells. Actually, LSCO is a Ruddlesden-Popper perovskites, that consist of 2D perovskite-like slabs interleaved with cations. This type of structure can be written as $\text{A}_{n+1}\text{B}_n\text{O}_{3n+1}$, where A and B are cations, O is the oxygen, and n is the number of octahedral layers in the perovskite-like slab. The number of CuO_2 layers in the cuprates refers to n, that in LSCO is equal to 1.

LSCO can be doped in two different ways, with chemical cation substitution and with intercalation of excess oxygen (see figure 2.3). In the undoped case, the parent compound La_2CuO_4 is a Mott insulator with orthorhombic cell, where there is one hole per Cu^{2+} cation. To minimize the exchange interaction the spins are arranged in an antiferromagnetic order, and due to the high on site repulsive potential electrons are strongly localized on the Cu site, hence the material is antiferromagnetic and insulating. The standard way to hole-dope La_2CuO_4 is to chemically substitute Sr^{2+} for La^{3+} cations, creating random substitution sites in the layers nearby the CuO_2 planes, as illustrated in figure 2.3(b). Due to the higher valence the Sr^{2+} cations attract electrons from the CuO_2 planes creating an effective hole doping [54]. Moreover, the unit cell become tetragonal. LSCO can also be hole-doped by introducing additional oxygen as the majority of cuprates [9]. However, in contrast to YBCO, where the exceeding oxygen is introduced in well defined positions in

the unit cell, along the $b - axis$ [55], in LSCO the extra oxygen are introduced in interstitial positions close to the apical oxygen between the LaO planes [56]. The raw formula of LSCO can be therefore written in a more complete way: $\text{La}_{2-x}\text{Sr}_x\text{CuO}_{4+y}$, where the doping is provided by both the Sr concentration and by the excess oxygen atoms. In the case of the pure Sr doping, the doping level p is equal to the strontium concentration x , while in case of oxygen co-doping the resulting doping will be a function both of the Sr concentration and the oxygen non-stoichiometry y , i.e. $p = f(x, y)$. T_c dependence on the doping is strong and non-monotonically increasing, resulting in a dome-like shape of the superconducting region in the phase diagram (as we will see in the next paragraph). In case of the combined Sr and O doping, the critical temperature presents a peculiar doping dependence. Experimentally it has been observed that films at the optimal doping of Sr (and beyond, $p > 0.16$) have a T_c which is independent of the excess of oxygen content; viceversa, fully oxygenated underdoped LSCO films ($y \gtrsim 4$) have a T_c which is maximum, and is independent of the Sr content¹ [9]. The increasing concentration of dopant has also another effect: in LSCO the out-of-plane $c - axis$ expands with both Sr and O increasing content [8, 57, 58]. The extra oxygen atoms are introduced between the spacer layers, close to the apical oxygen, causing the c -axis to expand. This is in contrast, for example, with YBCO where the oxygen has an adhesive effect, with the contraction of the out-of-plane c -axis with increasing oxygen concentration [55]. Indeed, in this case the oxygen are introduced along the b -axis causing the in-plane lattice parameter to expand, with a subsequent contraction of the out-of-plane one.

2.2.2 Phase diagram

The weak coupling between the CuO_2 planes, together with the possibility to dope the Copper oxide planes, give rise to a plethora of different orders and phases, that are well summarized in the phase diagram shown in figure 2.4, where they are plotted as a function of temperature and doping. The doping level in cuprates is commonly expressed as the number of hole per planar Cu atom, indicated as p , such as to allow a comparison between different cuprates with different doping mechanism. In $\text{La}_{2-x}\text{Sr}_x\text{CuO}_4$ ($y = 0$), p is simply equal to the substitution concentration x of Sr atoms. In $\text{YBa}_2\text{Cu}_3\text{O}_{7-\delta}$, instead, the relation between the doping p and the non-stoichiometry of oxygen δ is not linear ($\delta \neq p$) [59].

The undoped La_2CuO_4 is antiferromagnetic and insulating, below the Néel temperature T_N ². As holes are introduced in the copper oxide planes the material becomes metallic and superconductive below T_c . The critical temperature in cuprates depends on the doping: in LSCO, as in other cuprates, it has been found that the superconducting transition temperature has a parabolic relation [8, 60–62]:

$$1 - \frac{T_c}{T_{c,max}} = 82.6(p - 0.16)^2 \quad (2.1)$$

¹The terminology *underdoped*, *optimally doped*, *overdoped* is always referred to the strontium concentration x , with the optimal doping value of $p = x \sim 0.16$, corresponding to the maximum T_c .

²The Néel temperature T_N is the temperature above which an antiferromagnetic material become paramagnetic: i.e. the antiferromagnetic state is destroyed.

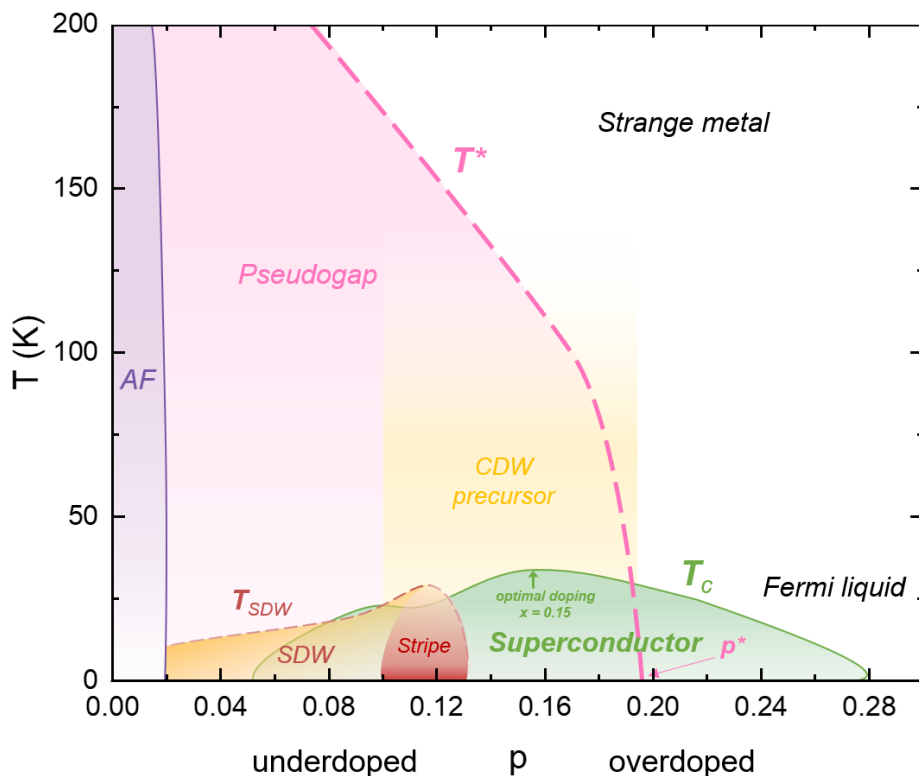


Figure 2.4: Temperature vs doping phase diagram of LSCO. The violet area is the antiferromagnetic order (AF) below the Néel temperature T_N , the pink area is the pseudogap phase below T^* , the yellow area is the charge density wave (CDW) precursor order, the orange one is the spin density wave (SDW) order below T_{SDW} , in red there is the stripe order region, and finally in green there is the superconducting phase below the transition temperature T_c . Adapted from ref. [3–5].

with the maximum $T_c = 39$ K around $p = 0.16$ which is called optimal doping. The regions for $p < 0.16$ and $p > 0.16$ are called underdoped and overdoped region respectively. The T_c deviates from the parabolic doping dependence around $p \approx 0.125$ where it is suppressed of about 11 K (5 K for the onset). The suppression of T_c , which is mainly a broadening of the superconducting transition, is commonly attributed to the competition between the superconductivity and the charge order that is strong in this doping range [5] (as it will be clarified in the following). In addition to superconductivity and charge order, the phase diagram is populated by a plethora of intertwined electronic orders and different phases, that will be discussed in details in the following sections.

2.2.2.1 Strange metal

At high enough temperature, the normal state of cuprates is called *strange metal*. This region is particularly pronounced at doping levels around the optimal one, where it extends from the highest attained temperature down to T_c . Since the discovery of high- T_c superconductivity in cuprates, this regime was quickly recognised as perhaps the most mysterious aspect of cuprates [22]. Cuprates here are called

"strange" metals, since they exhibit values of conductivity which are much lower than in normal metals, and show frequency and temperature dependence that cannot be explained with the standard model for conventional metals.

Normal metals are well described by the Landau's Fermi liquid theory, where the concept of quasiparticle is introduced. Briefly, a metal with many-body interaction can be described by substituting the many-body interaction with quasiparticle excitations with altered properties, such as the effective mass [63]. The most basic difference between the strange metal and a conventional metal is the absence of quasiparticles, as revealed by the absence of sharp quasiparticle peak in ARPES measurements [64]. This has some consequences on the physical properties of the system, for example on the resistivity. In normal metals, the resistivity saturate at high temperature when the mean free path become comparable to the de Broglie wavelength; at low temperature, instead, it presents a T^2 dependence as a consequence of the electron-electron interaction. In cuprates, the resistivity can be linear from near T_c up to as high the temperature measured [65], even when the inferred mean free path would be smaller: this would represent a violation of the Heisenberg uncertainty principle for the quasiparticles. Other signatures of the strange metal are the non-Drude like frequency dependence of the optical conductivity [66], and the temperature dependence of the Hall coefficient, that in a normal metal would become insensitive to temperature above $s\Theta_D$ (where $s \approx 0.2 - 0.4$ is a constant, and Θ_D is the Debye temperature).

Even though the phenomenology of the strange metal state has been successfully described by the so called Marginal Fermi liquid theory, a microscopic theory is still missing [67]. The main problem is to identify the scattering mechanism responsible for the linear dependence of the resistivity. One possibility to explain the strange metal behaviour can reside in quantum criticality [32]. A quantum phase transition (QPT) is a continuous phase transition occurring at zero temperature as a function of the doping (or in general a tuning parameter). The corresponding quantum critical point (QCP) defines the boundary between the ordered and disordered quantum phases [68]. There are signatures of a QCP within the superconductive dome at $T = 0$ K and $p = p^*$ (see figure 2.4) [69, 70]. However, these evidences are not conclusive. Furthermore, this quantum critical description should break down at higher temperatures, but the strange metal behaviour persist at the highest attainable temperatures.

On the overdoped side of the phase diagram the normal metallic behavior is recovered at low temperature with a gradual transition to the Fermi liquid regime [71]. On the underdoped side the strange metal phase ends by the opening of a *pseudogap*.

2.2.2.2 Pseudogap

The pseudogap region is present in the underdoped side of the phase diagram below T^* , and bounded between T_N and T_c . First discovered by ARPES as a partial gap in the low energy electronic spectrum [72], the pseudogap phase deepens the mystery around the normal state of cuprates, since its origin and the connection to superconductivity are still under debate [22, 73].

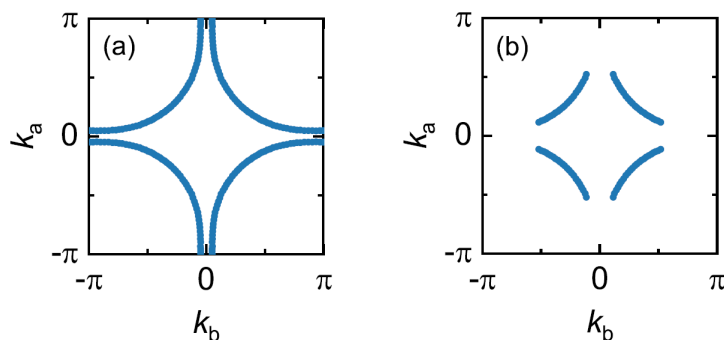


Figure 2.5: Schematic Fermi surface of the cuprates: (a) in the strange metal phase at room temperature, (b) Fermi arcs in the pseudogap phase below T^* . From ref. [2].

At high temperature the cuprate resides in the strange metal phase, where the Fermi surface is a large hole-like cylinder centered at (π, π) in the first Brillouin zone [14, 74] (see figure 2.5). As the temperature is lowered crossing T^* , the Fermi surface is gapped around the antinodal region, $(\pm\pi, 0)$ and $(0, \pm\pi)$, while the remaining Fermi surface is commonly referred to as Fermi arcs [75], as shown in figure 2.5. However, the Fermi surface of a material cannot abruptly end with open Fermi arcs. One possibility is that the Fermi surface is reconstructed to small pockets via zone-folding, due to a translational symmetry breaking associated to nanoscale orders. The Fermi arcs would be the front half of such pockets, but at present there is no evidence of it [76]. The structure of the pseudogap resembles the symmetry of the d-wave superconducting gap (see figure 2.2), which is maximum in the antinodal region [72]. Due to this similarity, it has been suggested that preformed Cooper pairs start to form already at the very high temperature T^* , but phase fluctuations prohibit superconducting order until much lower temperatures are reached.

Phenomenologically, the main signature of the pseudogap from transport measurements is given by the departure from the linear-in-T behavior characterizing the resistivity in the strange metal phase. Below the pseudogap temperature T^* , the resistivity - either presenting an upward or a downward curvature, based on the material - exhibits a quadratic dependence on the temperature [62, 77–79]. The pseudogap temperature T^* has a nearly linear dependence on the doping p in the underdoped side of the phase diagram, and it ends close to the doping level, where its value is very close to T_c $p^* \approx 0.18 - 0.19$ [80–82].

At present, the origin of the pseudogap is still unknown, and there is no unanimous consensus whether the pseudogap phase is a precursor or a competitor of the superconducting state [75, 83]. The picture is complicated by the presence of a plethora of different electronic phenomena arising at the onset of the pseudogap T^* , including electronic nematicity [84], loop currents [85], and charge order [2, 23].

2.2.2.3 Charge and spin order

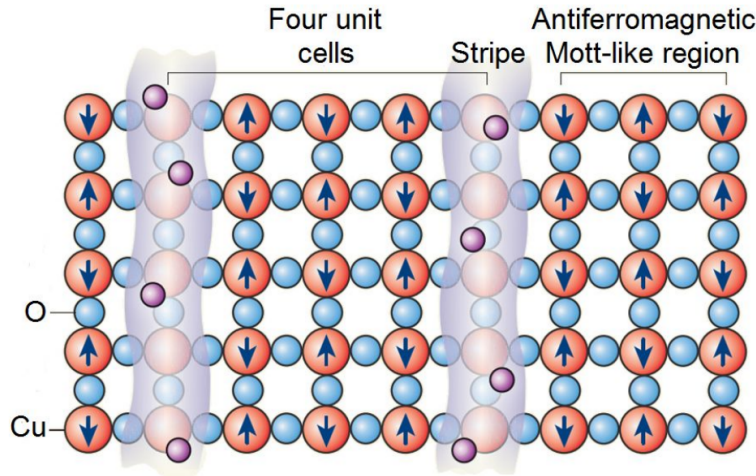


Figure 2.6: Picture of the stripe order in LSCO in CuO₂ planes seen from above. The antiferromagnetic Mott-like regions, where the spins are indicated by blue arrows, are separated by narrow rivers of mobile charge (purple circles). Adapted from [6].

The underdoped side of the phase diagram host a variety of symmetry breaking orders. Neutron scattering experiments in the mid-1990s led to the discovery of electronic "stripes" in underdoped LSCO [30]. In the stripe region, periodic spatial modulation of charge and spin density, are characterized by a well defined relation of periodicity. The charge carriers are confined in lattice-constant wide lines (stripes), spaced by antiferromagnetic regions of period $4a$ (see figure 2.6). The superconductivity phenomenon on each stripe can be explained by the confinement of charge carriers to one dimension. Approaching the critical temperature the carriers undergo spin-charge separation and superconductivity is established on each stripe due to a condensation of holons (spinless charge e bosons). Then, the stripes couple via the Josephson effect when $T = T_c$ and long range phase coherence is established. This stripe order is particularly intense at $p \approx 0.125$ where the T_c present a suppression with respect to the expected parabolic dependence vs doping. In a general sense, it came quite naturally to account for the diminished critical temperature assuming a competition between superconductivity and stripe order, but for many years static stripe order was considered an exclusive property of the LSCO family. However, lately static short range incommensurate charge order, the so-called charge density wave, was revealed by Resonant Inelastic X-Ray Spectroscopy (RIXS) also in other cuprates [23, 27, 86], but unlike in the LSCO family there is no evidence of an associated static magnetic order.

Charge density waves are incommensurate periodic modulations of the charge density in the CuO₂ planes (see figure 2.7), occurring in the phase diagram in the doping range $0.08 \lesssim p \lesssim 0.18$ [3]. They present a peculiar temperature dependence. Indeed, the CDW signal starts to build up at high temperature (see figure 2.4), to reach the maximum at T_c , and then remarkably drops below T_c : this occurrence denotes a

competition between the superconductivity and the charge order [23, 27].

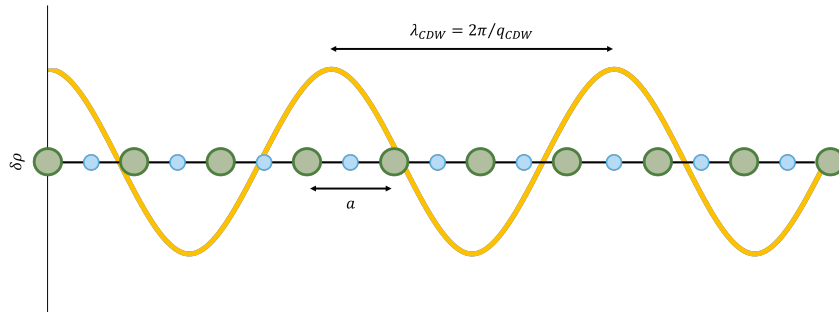


Figure 2.7: Simplified illustration of the incommensurate CDW in LSCO superimposed to one of the orientation of the CuO_2 planes seen from the side. The green and blue circles are Cu and O atoms respectively. $\delta\rho$ is the charge density deviation from the average value, a is the lattice parameter, and λ_{CDW} the wavelength of the CDW modulation.

The CDW are quasi-2D, with a correlation length along the c -axis almost negligible. The onset temperature T_{CDW} has dome-shape doping dependence with a maximum at $p \approx 0.125$ [3, 5, 87], while the CDW wavevector q_{CDW} normally decrease with the increasing doping concentration, as happens for YBCO [88] and Bi-based copper oxides [24, 89]. In LSCO, the variation of the CDW wavevector with doping has the opposite sign than in YBCO and Bi-based cuprates. However, in recent reports CDW correlation without spin-charge locking has been found in the LSCO family [90]. These CDW extend set up above the onset of the stripes, and are characterized by a shifting of the wavevector to higher values than q_{CDW} , violating the relation of periodicity with the spin fluctuations. Moreover, it has been found that the wavevector of these high temperature charge density fluctuations - precursor of the stripes - is not uniquely defined by the doping level [90]. These evidences pointed out how on one side the tendency to charge ordering seems universal among the cuprates, while on the other side the peculiarity of these charge modulations are not.

Connected to these precursors of the stripe, short-range dynamical charge density fluctuations were recently discovered [91]. The most intriguing founding is their ubiquitous presence (both in temperature and doping) among the phase diagram, persisting also above the pseudogap temperature T^* . Indeed, for their characteristics - presence in a broad range of the phase diagram, finite energy and short correlation length that implies a broad almost isotropic q -space distribution - they have been immediately connected to the strange metal phase of HTS. Besides the mere phenomenology, some theories, by extending perturbatively into the strange metal region the approach of a Fermi liquid, put the CDF at the origin of the strange metal phenomenon, since it can provide the scattering mechanism responsible for the linear resistivity [32, 92].

At low doping, another type of electronic order is present, the spin density wave order (SDW), that is a periodic modulation of the electronic spin density [28]. In the undoped compound the spins are localized because of the strong Coulomb interaction between the electrons on neighboring lattice sites. When the LSCO is doped the Néel temperature T_N goes rapidly to zero at $p \approx 0.05$, point at which the commensurate antiferromagnetic order is replaced by the incommensurate spin order.

There is also evidence of an exotic state in the cuprate phase diagram called pair density wave (PDW) [93]. The PDW is a periodic spatial modulation of the Cooper pair density with finite momentum [94]. Already discovered in $\text{La}_{2-x}\text{Ba}_x\text{CuO}_4$ (LBCO), the PDW order has been recently found also in BSCCO by scanning tunneling microscopy [95]. According to some theories, the PDW order is the prime candidate to explain the complex physics of the phase diagram of the cuprates [94]. Indeed, it is seen as the "mother" state from which the intertwined and competing orders such as charge, spin and superconductive orders originate [96]. Moreover, there are indications that PDW fluctuations may be responsible for the pseudogap phenomenology [94, 97]. However, the evidence is no yet conclusive.

3

Growth and characterization of LSCO ultra-thin films

The cuprates are extremely challenging materials to growth in thin film form. The crystallinity of the film and the specific structure of the unit cell strongly affect the transport properties of the films. In this chapter, we will start with a review of the main results which have been achieved over the last decades for the growth of thin films of LSCO. After that, we will describe the process of growth and optimization of the LSCO thin films we have followed. Finally, we will present the morphological, structural and transport characterization of the deposited films.

3.1 Growth of LSCO

In the past 30 years, LSCO has been intensively studied, both in bulk and thin film form. Despite the rather simple crystal structure, the growth of LSCO in thin film form demonstrated to be a challenging task. Several techniques were employed for the deposition of LSCO films. Since the second half of the 1990s, Pulsed Laser deposition (PLD) and Molecular Beam Epitaxy (MBE) have proven to be the most successful ones. In particular, the best results were obtained with MBE, where the highest level of stoichiometry control is achieved. By PLD is also possible to obtain good results, even if with a lower precision in the control of the stoichiometry.

In the earliest studies on HTS, a large effect of positive hydrostatic pressure on the critical temperature was found in LSCO bulk system [98]. This compressive pressure has a positive effect on the T_c , which increases with increasing pressure. This appeared therefore of relevance for thin films growth where the substrate, that has a lattice mismatch with respect to the film, induces an in-plane compressive or tensile strain. In this way is possible to study the effect of the elongation or contraction of the in- and out-of-plane lattice parameters on the superconducting properties. At the beginning, the most commonly used substrate for the growth of LSCO thin films was SrTiO₃ (STO). STO has a cubic cell with a lattice constant larger than the in-plane lattice parameter of LSCO: it induces therefore an in-plane tensile strain on the cell of LSCO. However, it was quickly noticed that this in-plane tensile strain has a negative effect on the T_c of LSCO. Several groups reported lower values of T_c in LSCO thin films on STO with respect to the bulk ones [99–101]. Moreover, LSCO films on STO show a significant reduction of the critical temperature with decreasing thickness of the film below 600 nm [100, 101]. To avoid this negative effect of the strain, Cieplak et al. used a different substrate

material, LaSrAlO_4 (LSAO), isostructural with LSCO, but with a shorter in-plane lattice constant, such as to induce an in-plane compressive strain on the deposited film. The T_c thickness dependence (decreasing of T_c for decreasing thickness of the film) is less pronounced in films grown under in-plane compressive strain with respect to films grown under in-plane tensile strain [101, 102]. Moreover, the LSCO films grown on LSAO have a much higher T_c than the one on STO, comparable to the one of the bulk, or even exceeding it [7] (see figure 3.1).

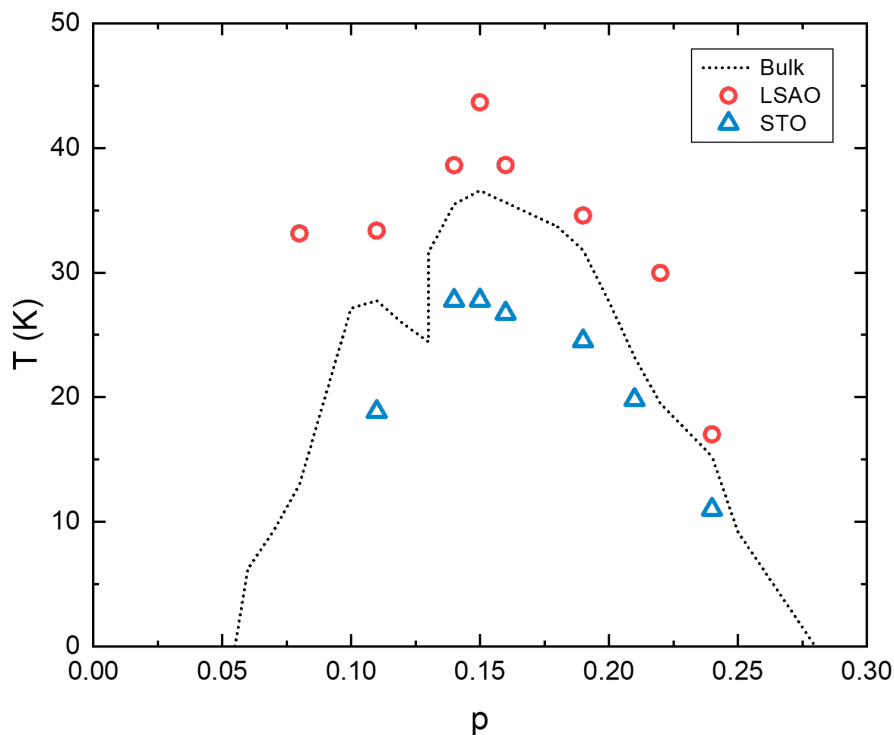


Figure 3.1: T_c of thin film of LSCO grown on two different substrates (STO and LSAO) subject to tensile and compressive strain, compared to the bulk T_c values. Red circles are T_c of films grown on LSAO, while the blue circles are T_c of films grown on STO from reference [7]. The dotted line represent the T_c of the bulk compound, from [8].

It has been argued that the enhancement of the superconducting properties can be linked to the expansion of the c – axis due to the Poisson effect [103]. This speculation was strengthened by another results obtained by MBE: in 1998 Loquet et al. succeeded in depositing 15 nm thick underdoped LSCO films on LSAO with an enhanced T_c of 49 K¹ [34]. In this work, not only the importance of the stoichiometry of the deposited material was emphasised, but also that of the defects and strain relaxation in the film, as well as that of the stacking sequence of the atomic layer at the interface. However, it has been argued that this huge enhancement of the T_c cannot be the result of the strain effect alone, and the expansion of the c – axis

¹This value must be compared with the bulk T_c of 25 K, corresponding to the same doping level of $x=0.1$ of the films reported in the paper.

can be explained also by the introduction of oxygen [58]. Indeed, it is well known that the critical temperature of LSCO thin films is very sensitive to the oxygen non-stoichiometry [9]. In particular, the intercalation of extra oxygen in underdoped LSCO lead to a considerable increase of the critical temperature, while this effect is reduced and almost negligible in optimally doped LSCO films [9, 58]. This effect can be explained using as starting point the mother compound of LSCO, La_2CuO_4 (LCO). LCO can be doped either with oxygen ($\text{La}_2\text{CuO}_{4+y}$) or with Strontium ($\text{La}_{2-x}\text{Sr}_x\text{CuO}_4$). Moreover, the T_c for optimally O-doped $\text{La}_2\text{CuO}_{4+y}$ is even higher than the one of the optimally Sr-doped LSCO [104]. Therefore, $\text{La}_{2-x}\text{Sr}_x\text{CuO}_{4+y}$

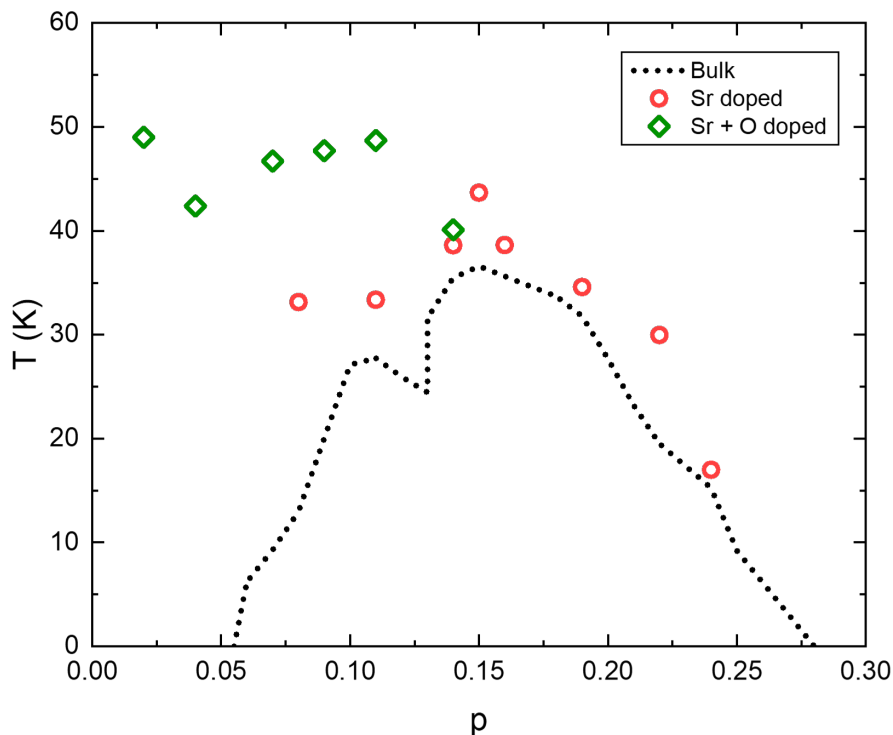


Figure 3.2: Oxygen and strontium co-doping effect on LSCO films. Adapted from reference [8, 9]

can be co-doped with both Sr and O. Co-doping underdoped LSCO with O results in a compound which seemingly follows the superconductivity of O-doped LCO, by having a critical temperature $T_c \approx 45$ K independent on the Sr concentration (see figure 3.2). The oxygen doping compensates for the Sr deficiency bringing underdoped LSCO to the optimally doped level. On the other hand, the effect of the oxygen co-doping in an already optimally doped LSCO film is weak and almost negligible. It has been also demonstrated that in principle it is possible to explore the entire phase diagram by changing the oxygen concentration of an underdoped LSCO film by post-annealing the films in an ozone rich environment [105]. Indeed, ozone has an oxidizing power six orders of magnitude larger than molecular oxygen [58], and it has been widely used to enhance the superconducting properties of LSCO films or to study the oxygen co-doping dependence of the T_c of LSCO. Nonetheless, since it is extremely complicated to disentangle the contribution of the oxygen and

strontium doping, and of the strain, on the critical temperature, it is legit to object that the ground state of $\text{La}_{2-x}\text{Sr}_x\text{CuO}_4$ and $\text{La}_{2-x}\text{Sr}_x\text{CuO}_{4+y}$ may be different. In other words, the phase diagram of oxygen co-doped LSCO may be different from that characterizing the Sr-doped one. For this reason the aim of this thesis work is the growth of optimally doped LSCO thin films by PLD, with T_c values comparable to the bulk values, without the use of in- or ex-situ ozone post-annealing.

Growing LSCO by PLD can be an extremely undertaking task. To our knowledge, there is only one previous work reporting LSCO films grown by PLD on LSAO single crystal [106], and few more of LSCO grown on STO with an LSAO buffer layer [107, 108], with a superconducting transition comparable to the bulk one in terms of critical temperature and width of the transition. In general, there is a large spread of T_c values in film grown by PLD. Moreover, it is worth noting that the largest spread of the results has been obtained in reports where untreated commercially available LSAO substrate were used [100–102, 109]. In these cases, the films presented deteriorated superconductive properties, with T_c lower than the bulk, and significantly broadened transition. These negative effects were found to be exacerbated in thinner films.

In the following the results of the growth optimization of optimally doped LSCO ultra-thin films will be presented and compared to the aforementioned references.

3.2 Choice of the substrate: LaSrAlO_4

In the last decades, it has been widely demonstrated that the superconductive properties of LSCO thin films can be tuned by a proper choice of the substrate, even exceeding the bulk T_c [9, 34, 100, 101, 107]. To obtain high quality thin films with a specific crystal orientation, substrates with lattice parameters close to those of the film are typically used. If not too large, the substrate/film mismatch can be exploited to induce a specific type of strain on the film (see figure 3.3).

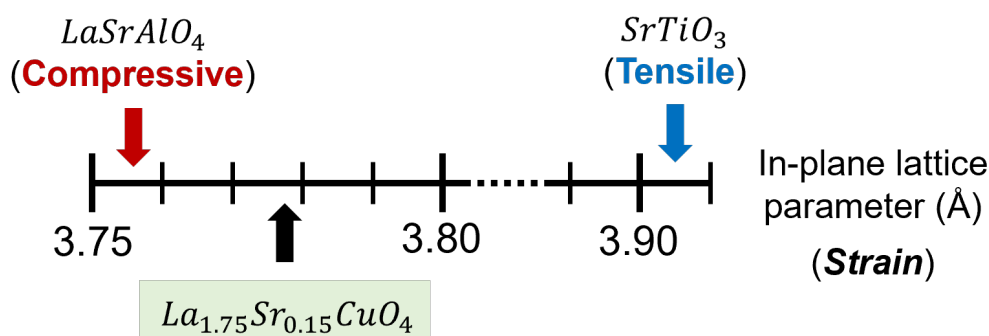


Figure 3.3: Quick illustration of the difference in in-plane lattice parameter of the substrates LSAO and STO compared to LSCO, with consequent type of strain induced.

The most commonly used substrates for LSCO growth are: SrTiO_3 (STO) with a cubic structure of lattice constant $a_{\text{STO}} = 3.905 \text{ \AA}$, and LaSrAlO_4 , isostructural with LSCO, and with an in-plane lattice constant $a_{\text{LSAO}} = 3.756 \text{ \AA}$. In the STO case,

the lattice constant is 3% larger than optimally doped $\text{La}_{1.85}\text{Sr}_{0.15}\text{CuO}_2$ ($a_{\text{LSCO}} = 3.777 \text{ \AA}$ for optimally doped LSCO), thus inducing in-plane tensile strain that, for the Poisson effect, shrinks the out-of-plane lattice constant c and commonly causes the reduction of the critical temperature [7]. In contrast, the LSAO in-plane lattice parameter is 0.5% smaller than LSCO. This causes the elongation of the c axis and tend to increase the T_c of the films [7, 58]. The thickness of the film is another parameter that can be used to tune the strain on the film. As the thickness of the film increases, the strain gradually relaxes and the effect of the substrate/film interface on the structural and transport properties diminishes.

For the purpose of this thesis, we have grown optimally doped LSCO films of 15 u.c. on LaSrAlO_4 (001) substrate to maximize the effect of compressive strain. Here, it is worth noticing that the strain is instrumental to modify the ground state of LSCO, and shed light on the intricate physics described in the previous chapter. The epitaxial strain induced by the substrate has been used in recent years to control the atomic positions and therefore the strengths of the interactions. Strain in cuprate HTS allows to control not only the critical temperature, as previously mentioned [[7, 34, 58]], but also the magnetic-exchange interaction [110] and the charge density waves [111–113]. As discussed in the previous section, in LSCO there is a strong thickness dependence of the T_c . In-plane tensile strain (i.e. using STO) on 15 u.c. thick films would have led to an excessive degradation of the superconductive properties [100]. Although the degradation of T_c by reducing the thickness is still present also in films grown on LSAO, the effect is much more weakened with respect to STO [101].

3.2.1 Substrate treatment and characterization

We used two different batches of substrates, respectively purchased from CRYSTAL GmbH in Berlin (Germany), and SurfaceNet GmbH in Rheine (Germany). The CRYSTAL substrates were double-side polished $10 \times 10 \times 0.5 \text{ mm}^3$, that we cut in $5 \times 5 \text{ mm}^2$ sized chips with a dicing saw. The SurfaceNet ones were instead one-side polished $5 \times 5 \times 0.5 \text{ mm}^3$. It is well known that in LSCO films the quality of the substrate surface is critical to obtain good superconductive properties in the films, and that the substrate surface condition can introduce an additional huge factor of variability in the resulting films [11].

To this purpose, we have tried several different substrates treatments to increase the reproducibility of the results, including Ar^+ ion etching, chemical etching, O_2 plasma ashing, and annealing. In figure 3.4 we report the result of AFM measurements for the optimized annealing process, which led to the best surface condition among the tested processes. The substrates were first cleaned with cyclopentanone for 5 min in ultrasonic bath (USB), wiped with cleanroom paper while rinsed with isopropanol, and then annealed for 3 h at a temperature of $950 \text{ }^\circ\text{C}$.

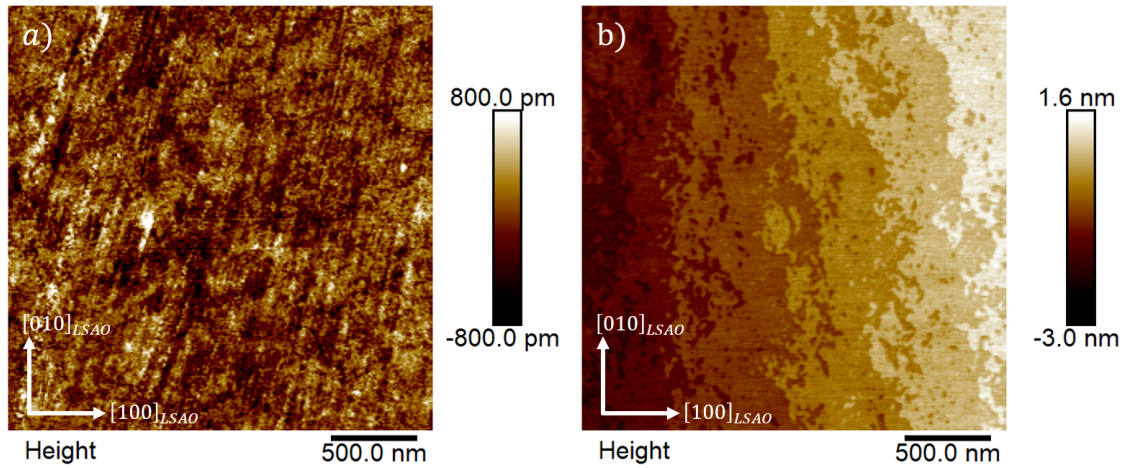


Figure 3.4: AFM image of the S06 LSAO substrate surface: a) before any treatment, b) after annealing for 3 h at 950 C.

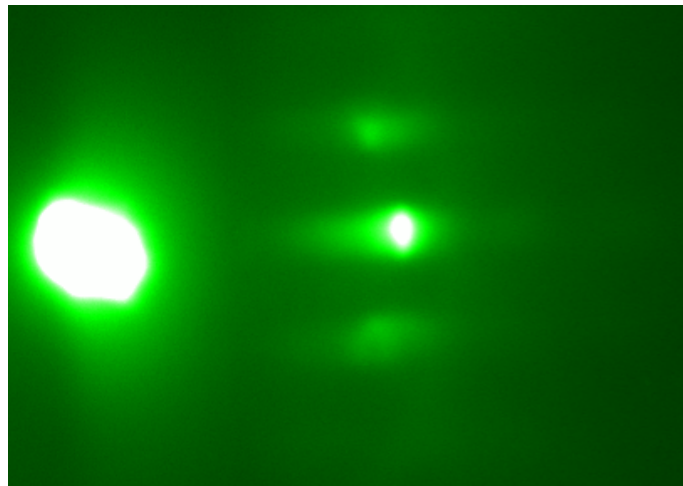


Figure 3.5: RHEED diffraction pattern of one of the SurfaceNet LSAO substrate. The strong specular spot, and the streak-like side spots indicate a flat surface.

As it is visible from the AFM image after the treatment we obtain an atomically flat surface, with steps of height $\approx 6 \text{ \AA}$ corresponding to half unit cell of LSAO. Moreover, the Reflection High Energy Electron Diffraction (RHEED) pattern is consistent with the AFM measurements, where the presence of the specular and side spots indicate a flat surface. The RHEED technique and its significance will be discussed in more details in the following section.

3.3 Pulsed Laser Deposition assisted by RHEED

LSCO, and cuprates in general, are layered multi-component compound and their epitaxial growth present several challenges to face. Since the compound transport properties strongly depend on the ratio of different elements, obtaining a deposited

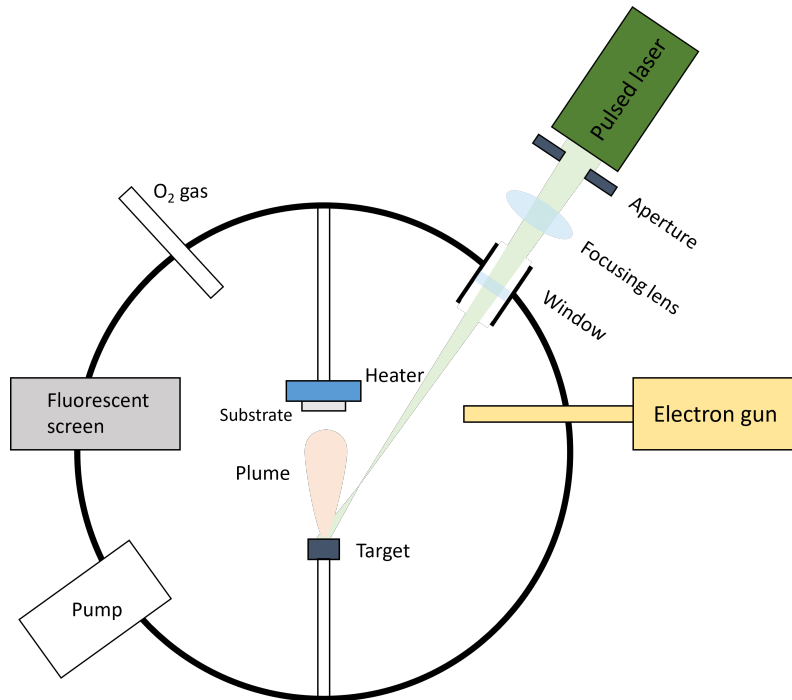


Figure 3.6: Scheme of the pulsed laser deposition system and the RHEED system used to monitor the growth.

film with the correct stoichiometry is of crucial importance. Another key challenge is to get films with smooth surface and high crystalline quality, which is a critical requirement for fundamental studies of the material and the fabrication of high quality nanodevices.

In the present work LSCO ultra-thin films were grown by pulsed laser deposition method. PLD is one of the most widely used techniques for the epitaxial growth of multicomponent materials, due to its ease of use and the preservation in depositing materials of complex stoichiometry. The main advantage of PLD derives from the material removal mechanism: in PLD an excimer laser is focused on a target, resulting in the ablation of some material. The ejected atoms, ions, molecules, and clusters form the so-called *plasma plume*. In a simplified picture, one can consider the ejection of the material to occur due to the target superheating, giving rise to a rapid explosion. In contrast to thermal evaporation, where the vapor composition is dependent on the vapor pressure of the elements present in the target, the laser-induced plasma plume has a similar stoichiometry to the target. In general, the PLD is the easiest way to obtain a film with the desired stoichiometry. However, as discussed in section 3.1, in PLD is not possible to have a complete control on the deposition dynamics, moreover there are several parameters affecting the growth of the film. The laser fluence (E), the pulse repetition rate (f), and the background oxygen pressure (P_{dep}) during the growth mainly affect the size and the shape of the plume. The substrate temperature (T_{dep}) during deposition, and the distance between the target and the substrate (d_{TS}) mainly influence the kinetics of the deposited atoms.

In addition, in our PLD an electron gun was available to monitor the film growth by

reflection high energy electron diffraction (RHEED). RHEED is a surface-sensitive technique that uses a highly collimated electron beam of energy 10-100 KeV that irradiates the substrate surface at a grazing angle. The electrons are then scattered and collected by a photoluminescent screen inside the chamber, creating a diffraction pattern. The pattern is the result of the intersection between the Ewald's sphere, which represents the allowed scattering condition for the electrons, and the reciprocal lattice rods of the crystal surface. Different crystallinity of the surface give rise to different rods in the reciprocal space, resulting in different RHEED patterns, as shown schematically in figure 3.7.

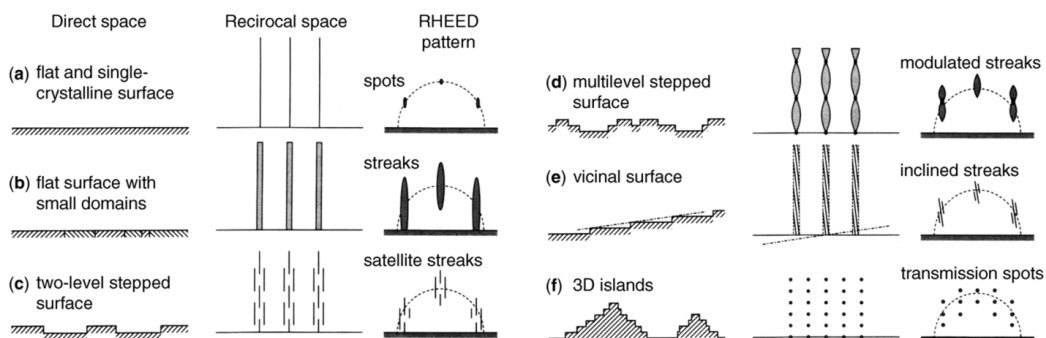


Figure 3.7: Schematics of different types of surface, in real-space morphology, in reciprocal space, and their RHEED pattern. Adapted from reference [10].

Therefore, it is possible to retrieve useful information about the surface quality from the RHEED pattern. Moreover, the intensity of the spots oscillates in time during the deposition of the film. Each time a unit cell layer is deposited (half unit cell in the case of layered structures as LSCO) the intensity of the signal is partially recovered. Useful information can be understood observing the intensity of the spots as a function of time: the deposition rate of the film, to determine the deposition time for a given thickness, and the growth mode of the film, as an indication of the effectiveness of the growth parameters.

3.4 LSCO film characterization

$\text{La}_{1.85}\text{Sr}_{0.15}\text{CuO}_4$ ultra-thin films were grown on LaSrAlO_4 (001) by PLD using an KrF excimer laser ($\lambda = 248$ nm). The Temperature during the deposition (T_{dep}) and the oxygen partial pressure (P_{dep}) were set to 750 °C and 0.1 mbar respectively. The laser energy (E), and the spot size of the laser (A_{spot}), defining the energy density of the impinging beam on the target $E_d = E/A_{spot}$, together with the target-substrate distance (d_{TS}), were kept as free parameters for the optimization of the growth conditions. All film thicknesses are set constant at 200 Å, except for one sample of 500 Å used for the nanowires fabrication. The thickness was calculated from the

RHEED oscillations during the growth, and then confirmed by X-ray reflectivity (XRR) measurements. The surface morphology was characterized with AFM measurements, while the structural quality of the film was evaluated by X-ray diffraction (XRD), and XRR. Transport properties were measured with a Physical Property Measurement System (PPMS), from room temperature down to $T = 5$ K. Finally, some of the samples were post-annealed at 150 °C in an ozone-rich environment at ambient pressure, for a duration up to 3 h, to determine the effect of excess oxygen in our films.

3.4.1 RHEED

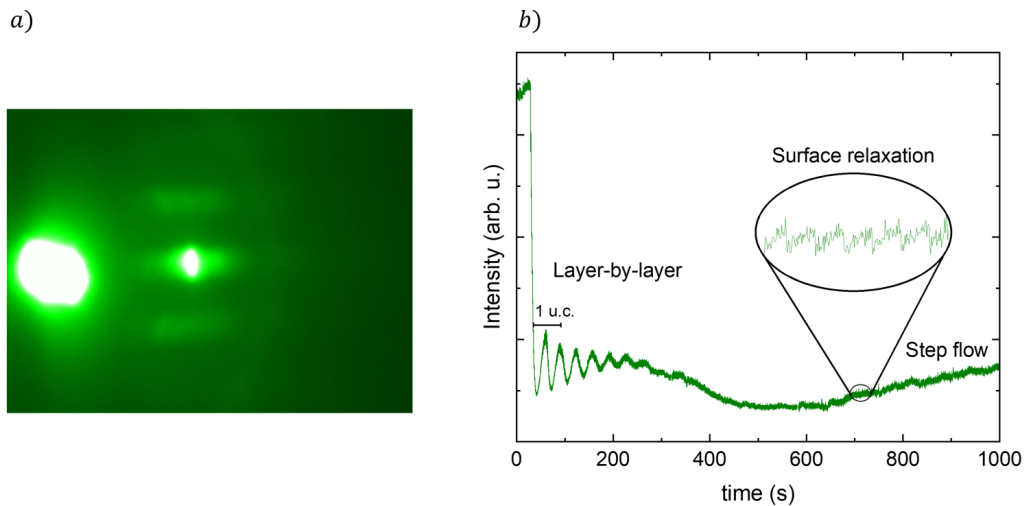


Figure 3.8: a) RHEED pattern of one LSCO film after the deposition. b) Intensity as a function of time of the central spot of the RHEED pattern during the growth. The signal is magnified in the inset to highlight the surface relaxation characteristic of the layer-by-layer and step flow growth mode.

In figure 3.8a) the in-situ RHEED pattern of a representative LSCO film after the growth is shown. As discussed in the previous section, the presence of one intense spot is the indication of a 2D surface. However, the slightly streak-like elongation of the peaks may indicate a marginal presence of small crystal domains on the surface. In figure 3.8b) the intensity of the RHEED pattern monitored during the growth is reported. During the first part of the growth, the intensity oscillations characteristic for the layer-by-layer (LBL) growth mode were observed. From the oscillation it has been possible to retrieve the grow rate of the film, and estimate the deposition time to deposit 15 unit cells. Since LSCO is a layered perovskite, the intensity of the RHEED signal is partially recovered each time half an unit cell is deposited, therefore two oscillations of the RHEED pattern correspond to one unit cell deposited. In the final part of the deposition, the growth mode changes from LBL to step flow (SF). At high deposition temperature, the adatoms have energy

high enough to migrate across the surface terraces before encountering other adatoms or starting to nucleate in islands. Step flow growth occurs when the adatoms have diffusion length larger than the terraces size, such that the adatoms find several favourable attachment sites on the step edge of the terraces. This causes the step front to propagate, leaving a very smooth atomically flat surface with a terrace-like structure. It is worth noting that the surface relaxation at each laser pulse can be observed during the entire deposition process, indicating a high quality of the growth. In particular, it also confirms that the actual growth mode of the film during the last part of the film is SF and not 3D growth. At each laser pulse, the ablated atoms arrive to the substrate/film surface in random positions, causing the intensity of the signal to drop (see inset in figure 3.8b)). Then, the atoms diffuse on the surface and eventually thermalize in atomic lattice sites, contributing to the diffraction pattern and therefore causing the signal to recover its intensity.

3.4.2 Surface

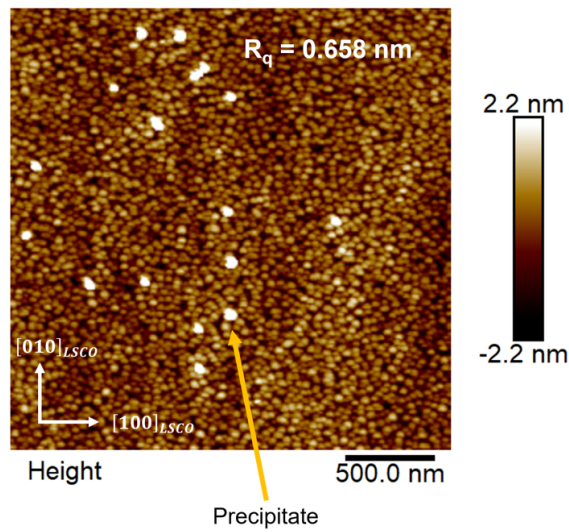


Figure 3.9: AFM image of the surface of one of the films after the deposition. Despite the presence of precipitates (indicated by the arrow) on the film, the surface is flat with a low roughness value R_q . The image was taken in tapping mode.

The surface quality of the films was determined with the AFM in tapping mode. AFM is a powerful instrument that allows the construction of a 3D map of the surface of the sample, giving quantitative and qualitative information about the surface, in terms of roughness, presence of precipitates or particles, and 3D islands. For each film, the surface was measured ex-situ after the deposition, to avoid possible contamination due to a prolonged exposure to air. In figure 3.9 the image of the surface of one representative sample is shown. The roughness value of the surface

(R_q) is small, $R_q \sim 0.6$ nm, corresponding to a flat surface and confirming the evaluation of the surface performed with the RHEED. However, one can notice the presence of precipitates of width ~ 50 nm on the surface, indicating an excess of some of the constituent element of the film, that probably increase the roughness of the surface.

3.4.3 Crystallinity

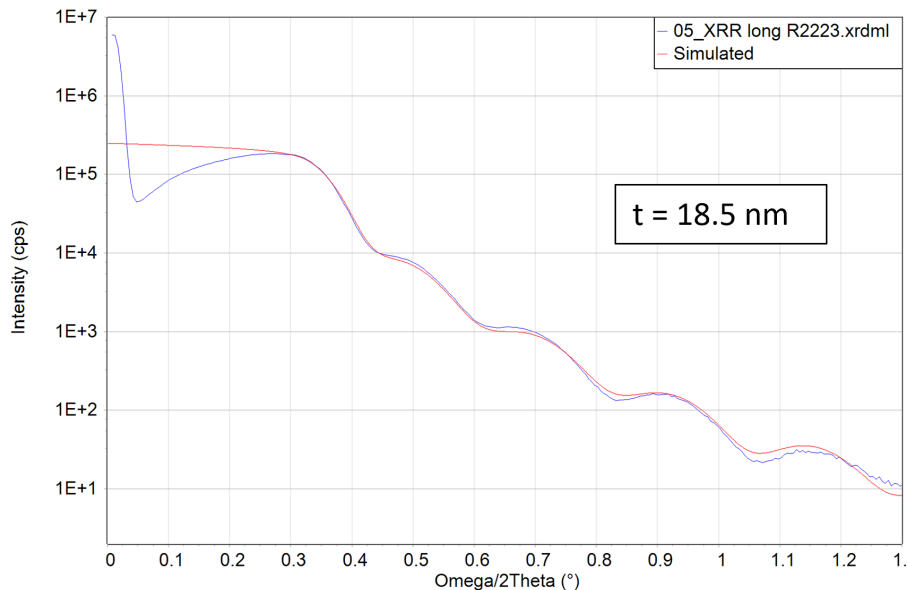


Figure 3.10: X-ray reflectivity measurement of one representative LSCO film. The scan is centered at the critical angle of the surface. The blue line represent the experimental data of the XRR profile of the film, the red line is the fitted curve. The estimated thickness of the film is shown in the box.

To further verify the surface quality of the films, specular x-ray reflectivity (XRR) measurements were performed. The quality of the crystal structure of the film was instead investigated by x-ray diffraction (XRD) measurements. The XRR measurement of one of our film is reported in figure 3.10. XRR is a surface-sensitive scattering technique, that allow to retrieve useful information about the surface roughness and the thickness of thin films. In XRR the sample is irradiated by a monochromatic X-ray beam at a glancing angle, and the X-ray intensity profile is monitored along the specular direction (i.e. the glancing angle and the exit angle are equal). In multilayered samples, the X-ray are partially reflected at each interface, creating an interference pattern called Kiessig fringes (see figure 3.10). From the period of these oscillations is possible to estimate the thickness of the film, while the intensity of the oscillations is related to the roughness of the surface. From the data fit, we estimated a thickness $t \sim 18.5$ nm. This value is in very good agreement with the value predicted from the RHEED oscillations. The small mismatch between these values (about 1 u.c. layer) is due to a possible change of the growth rate when the growth mode changes from LBL to SF. Moreover, the intense Kiessig fringes confirm once again the excellent quality of the surface.

In figure 3.11 the X-ray diffraction characterization of a LSCO film is presented. In XRD the photons are scattered by the regular array of atoms creating an interference pattern. The interference is constructive along specific directions determined by the Bragg's law, giving rise to peaks in the diffraction pattern. This diffraction pattern can be obtained monitoring the intensity profile of the diffracted X-ray, keeping the angle between the incident beam and the surface (ω) equal to the angle between the incident beam and the detector (2θ). The so-called $2\theta - \omega$ scan gives information about the crystallinity of the sample. Moreover, it is useful to investigate the presence of spurious peaks due to unwanted secondary phase in the film. In addition, it is possible to retrieve more accurate information about the mosaicity of the film performing an ω scan. In this case the detector is fixed at the angle where

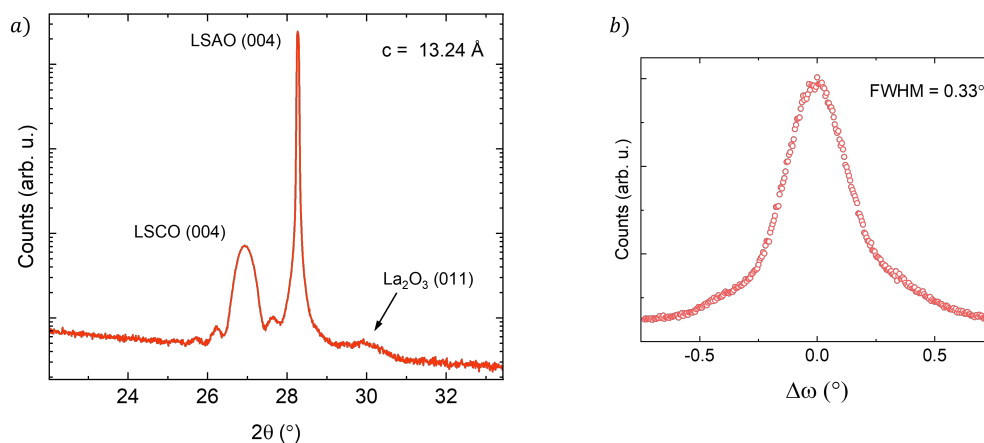


Figure 3.11: a) $2\theta - \omega$ symmetric scan of the LSCO (004) and LSAO (004) reflections. It is possible to note the presence of a smaller extra peak, corresponding to the La₂O₃ (011) reflection. b) Rocking curve of the LSCO (006) reflection. The FWHM of the peak is reported on the top right part of the plot.

the Bragg reflection is expected and the sample is tilted, recording the intensity of the diffracted X-ray as function of ω . The resulting peak is called rocking curve. The width of this peak depend on the degree of alignment between different crystal grains of the thin film. A narrow peak correspond to well aligned c -axis orientations. Figure 3.11a) shows a symmetric $2\theta - \omega$ scan around LSCO (004) reflection. From the position of this peak, together with those of the other (00n) peaks in the range 10°-80° (3.12) it has been possible to estimate the out-of-plane lattice parameter $c = 13.24 \text{ \AA}$, confirming that the film is actually under compressive strain (in the bulk $a_{LSCO} = 13.226 \text{ \AA}$). Moreover, it is possible to note the presence of a small peak corresponding to the La₂O₃ (011) reflection. We have associated the presence of this peak with the presence of precipitates on the surface observed with the AFM (see figure 3.9). Figure 3.11b) show the rocking curve of the LSCO (006) reflection. The peak is quite sharp, with a FWHM ≈ 0.3 was similar for all the films which have been deposited. Although sharp, the rocking curve is broader that in other LSCO films reported in literature at the same thickness [101, 107]. This broadening could be due to the presence of the precipitates in the film, that may induce a higher

degree of disorder.

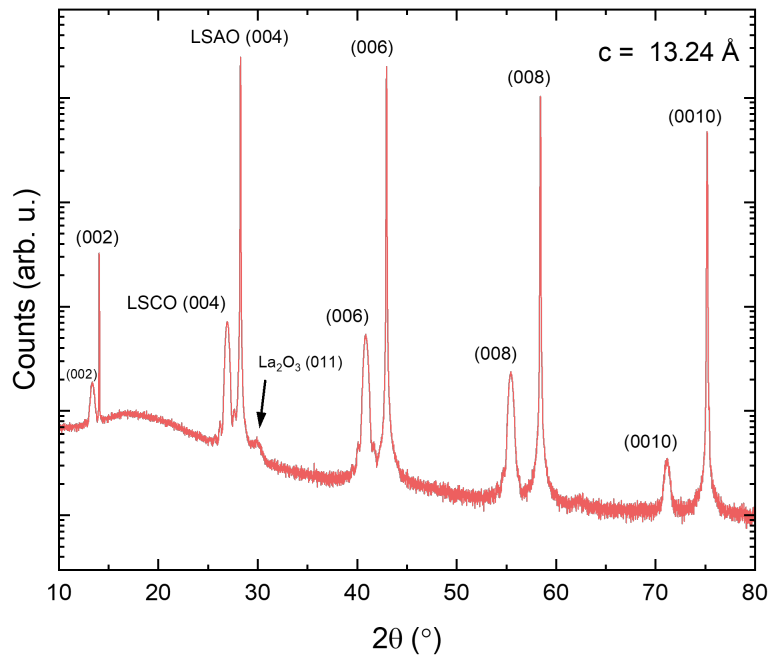


Figure 3.12: $2\theta - \omega$ symmetric scan of the LSCO (00n) and LSAO (00n) reflections in the range 10° - 80° . The smaller reflection peak belong to LSCO, while the higher in intensity to LSAO. The out-of-plane c parameter estimated from the bragg peak position of LSCO (is reported in the top right part of the plot).

3.4.4 Electric transport

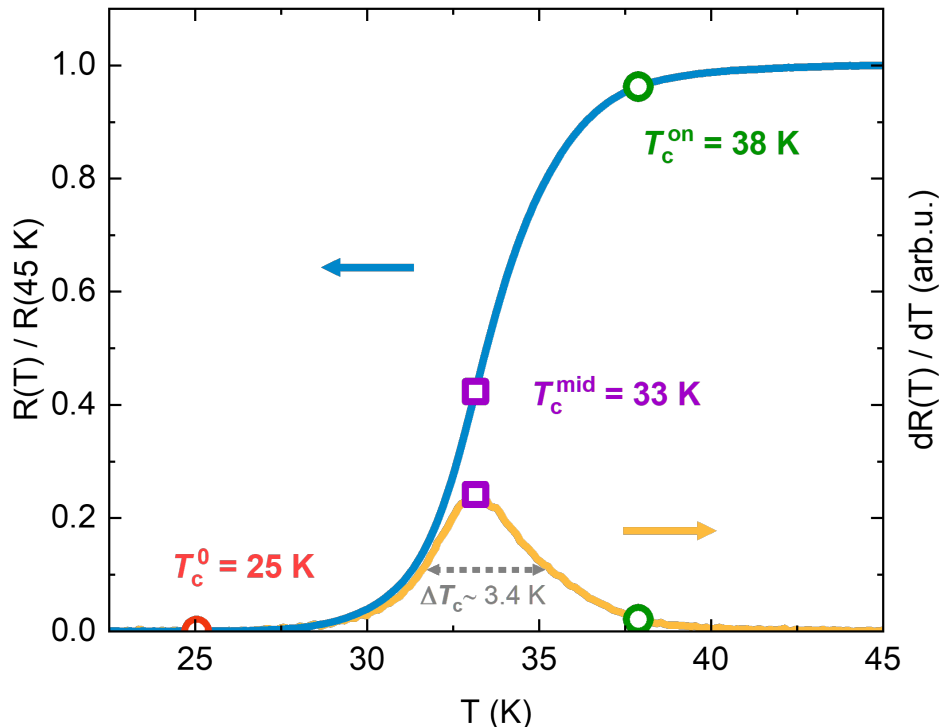


Figure 3.13: In-plane $R(T)$ normalized at 45 K, and $dR(T)/dT$ around the superconducting transition for one of the best obtained film. The onset of the transition, defined as the 10% of the first derivative is reported in green. In purple the midpoint of the transition, defined as the maximum of the first derivative. In red the T_c^0 , defined as the temperature at which the resistance completely vanish. The width of the transition is reported in gray, defined as the FWHM of the first derivative.

The transport properties of the films were measured with a Physical Property Measurement System (PPMS). The resistance was studied from room temperature down to 5 K. The samples were measured in Van der Pauw geometry, bonded with aluminum wire. Silver paint was placed on the bonds to improve the electrical contact and reduce the noise introduced by a high contact resistance.

In figure 3.13 the $R(T)$ normalized at its value at 45 K is shown for one of our best film in the temperature range around the superconducting transition, together with its first derivative. The T_c^{on} , defined as the 10% of the first derivative, is about 38 K. However we obtain a midpoint of the transition T_c^{mid} about 33 K, defined as the maximum of the first derivative, and a T_c^0 of 25 K defined as the temperature value at which the resistance completely vanish. The width of the transition, defined as the FWHM of the first derivative, is 3.4 K. Our results are comparable with the reference values for the bulk compound [8], where $T_c^{\text{on}} \approx 39$ K and $T_c^{\text{mid}} \approx 37$ K.

However, the transition is broader with respect to the bulk one. As already discussed in section 3.1, several groups have reported broadened transition in the thin films. It can be due to the presence of oxygen vacancies, or to the higher degree of disorder of the film under strain with respect to the bulk. In particular, comparing our results with previous work, for films of similar thickness (10 nm), and where the stoichiometry of the film has been confirmed by Rutherford backscattering, similar values of $T_c^{\text{on}} \approx 40$ K and $T_c^0 \approx 25$ K for optimally doped LSCO films were reported [114]. Hence, it is reasonable to assume that our best films are optimally doped, since the broader transition can be due to the structural properties of the film rather than the stoichiometry. We shall give further confirmation of the stoichiometry of our best films in the following section.

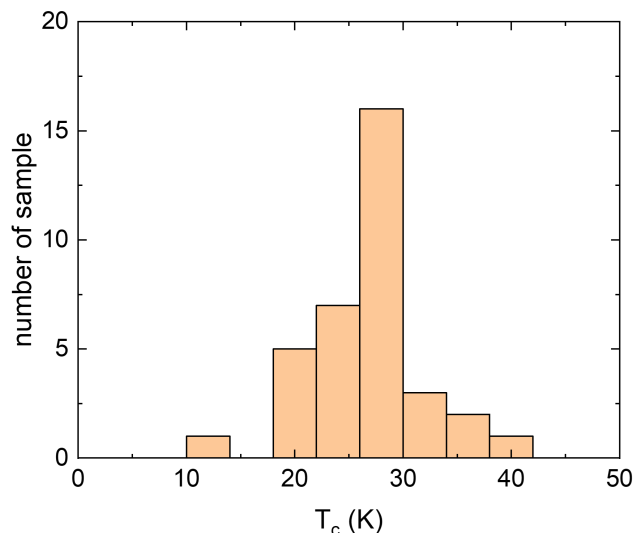


Figure 3.14: Histogram for T_c of our superconducting LSCO films.

However, in general we have obtained a spread of the T_c values for our films. In figure 3.14 a histogram of the T_c of our superconducting samples is presented. This is a well-known problem in LSCO films also grown by MBE. In figure 3.15 a similar histogram showing the spread of the T_c of LSCO films grown by MBE is shown from reference [11]. In this work, the crucial importance of the substrate surface quality for the growth of LSCO film has been reasserted. Indeed, a large spread of the T_c of LSCO films grown on untreated LSAO (figure 3.15a)) was observed. In this case, the spread of the results was reduced after chemical etching of the LSAO substrate with a methanol solution of hydrochloric acid (HCl), even if this chemical etching process does not produce single-terminated LSAO surface. We have tried to repeat the process for our samples, but unsuccessfully, on the contrary the chemical etching has considerably deteriorated the surface of the substrate. The reason of the difference between our result and that of ref. [11], concerning the chemical etching process, is still under investigation.

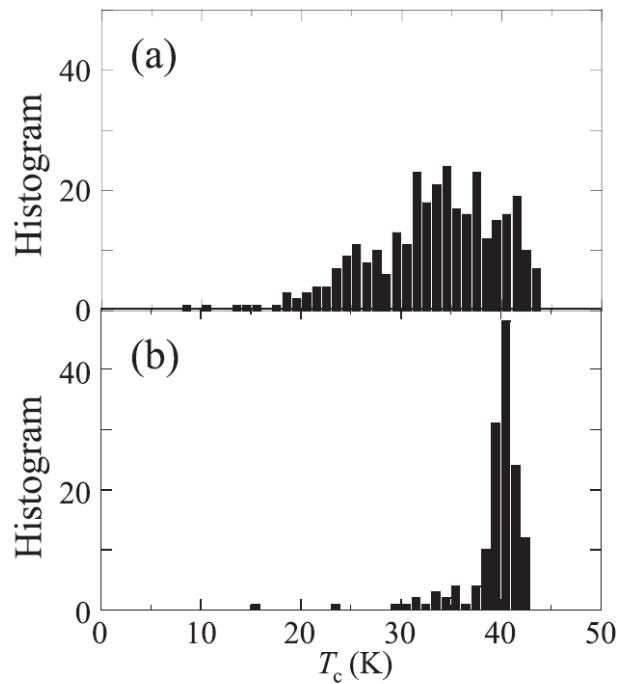


Figure 3.15: Histogram for T_c of optimally doped LSCO film grown by MBE with thicknesses between 50 and 5000 Å on LSAO cleaned a) by organic solvent and b) by chemical etching with methanol solutions of 1 vol.% hydrochloric acid (HCl). From reference [11].

3.4.5 Ozone post-annealing

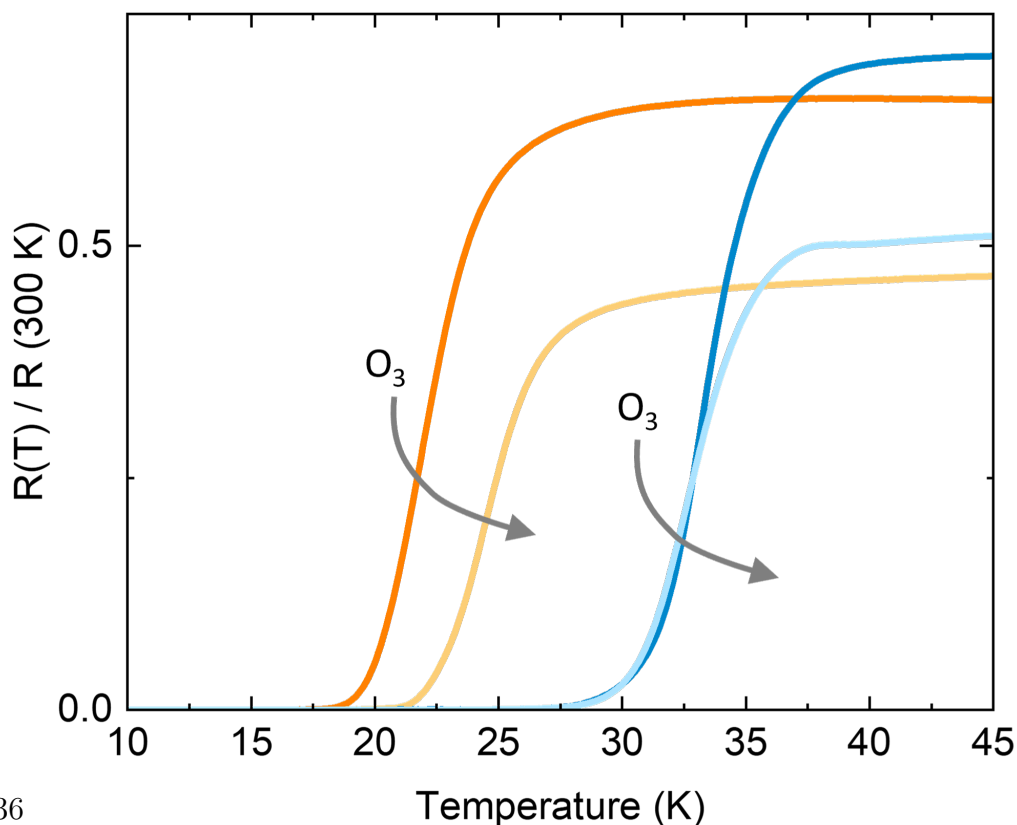


Figure 3.16: Effect of the ozone post-annealing on two samples. The orange line is one sample representative for the "low T_c " films before the post-annealing in ozone, while the yellow line is the same sample after the post annealing. The blue and

To further confirm the stoichiometry of our sample with the highest T_c , we have studied the effect of ozone post-annealing. As discussed in section 3.1 in LSCO it is well known that the intercalation of excess oxygen contribute to the doping enhancing the critical temperature. However, this effect is more pronounced in underdoped LSCO, where the change in T_c is remarkable. On the other hand, in optimally doped LSCO the T_c is almost insensitive to the extra content of oxygen. Therefore, post-annealing a LSCO film in a highly oxidizing atmosphere will result is a large change in T_c for an underdoped film, while the change in T_c for an optimally doped will be negligible. In previous reports a mixture of ozone and molecular oxygen is often used, since it is known that the oxidizing power of ozone at low temperature is higher than that of molecular oxygen by a factor of more than 10^6 [58]. We have post-annealed some films with lower critical temperature and one of the best film with higher critical temperature in an O_3/O_2 mixture. It has been demonstrated that such temperature is high enough to fully oxidize underdoped LSCO [58]. Moreover, we have previously demonstrated the effectiveness of this process in considerably increasing the oxygen content in YBCO thin films and nanostructures [115, 116]. The post-annealing was carried out in a system consisting in a chamber with a constant O_2 flow, where the sample was placed on a hotplate at 150°C . Ozone was generated by UV radiation emitted by a mercury lamp embedded in the system, that was kept active also during the cooldown of the sample. The samples were post-annealed for 3 h plus the time to cooldown the sample to room temperature of about 45 min (the warm up time is negligible since the sample reached 150°C in few minutes). The results are summarised in figure 3.16 for one of the best film and for one of the films with lower T_c . In the case of the film with lower T_c the critical temperature changed considerably, while in the film with higher T_c the effect of the annealing was absent. This, together with the comparison of the T_c values with reference where the stoichiometry was confirmed by Rutherford backscattering ([114]) bring to the conclusion that our films with the highest T_c are actually optimally doped LSCO films.

4

Nanowires fabrication

In order to probe the ground state of cuprate HTS, characterized by the presence of nanoscale orders as the stripe for LSCO or the CDW for YBCO, the fabrication of high-quality nanostructure with dimensions comparable to the characteristic lengthscale ($\sim nm$) of this nanoscale orders is required. However, the realization of nanostructures preserving properties close to the bulk material is an undertaking challenge for HTS cuprates. The reason has to be found in the chemical instability of these compounds, that are prone to oxygen-out-diffusion, and in the extreme sensitivity to defects and inhomogeneity due to the very short coherence length ξ , in the order of few nm. In particular, nanopatterning of LSCO has turned out to be an extremely demanding process. To our knowledge, there is only one report of an attempt of fabrication of LSCO nanowires [36]. However, the values of the critical current density of their nanowires is about 1×10^8 A/cm², exceeding the theoretical limit for the depairing current predicted by the Ginzburg-Landau (GL) model. Moreover, although they had at their disposal probably the best quality LSCO film worldwide, they did not managed to obtain working nanowires with width smaller than 300 nm, possibly due to the degraded quality of the devices after the fabrication process [36].

In this thesis work we have successfully used Electron Beam Lithography (EBL), in combination with an an amorphous hard carbon mask, and a soft Ar⁺ ion etching to realize LSCO nanowires with cross section down to 50×50 nm². The parameter of the fabrication process are discussed in the appendix ???. In the following, the main steps of the improved nanofabrication process, already successfully used for other cuprates [12, 13, 117], will be described.

4.1 Fabrication steps

The superconducting properties of the nanostructure are strongly affected by the choice of the masking material, the resist backing temperature, and the ion milling etching parameters. Although these parameters have been optimized for YBCO, they have been proved to be optimal also other cuprates such as Pr_{2-x}Ce_xCuO_{4- δ} (PCCO) [12, 13, 117]. With reference to figure 4.1 the main steps of the nanowires fabrications are the following:

1. deposition of the film (discussed in chapter 3)
2. Right after the deposition the LSCO film is coated ex-situ by a 50 nm gold (Au) capping layer.
3. A 100 nm thick hard carbon (C) layer is used as mask. Since carbon is very

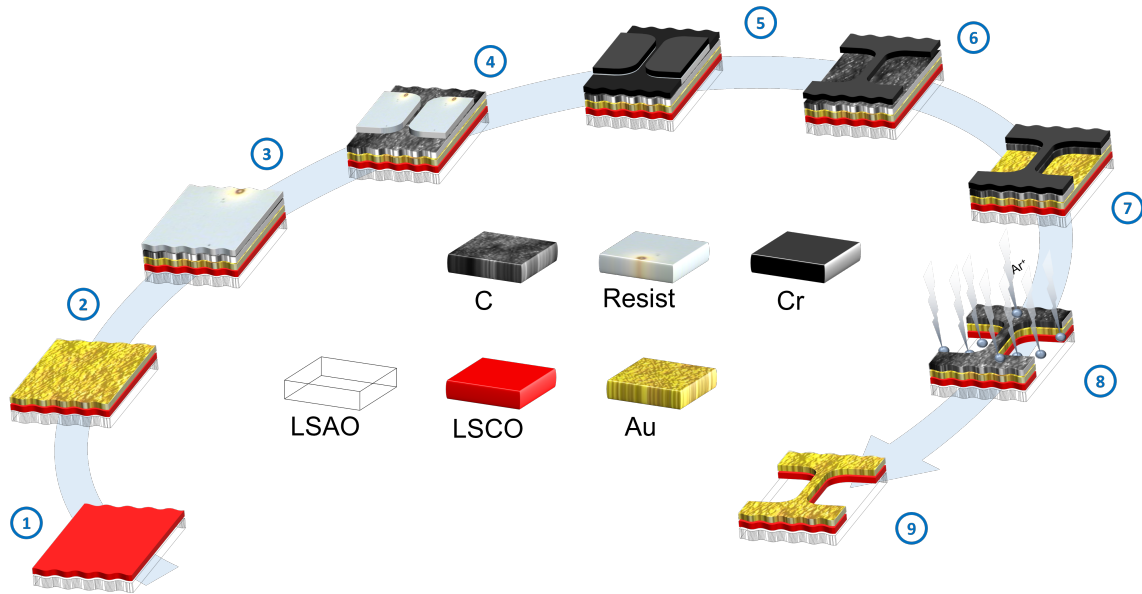


Figure 4.1: Schematics of the fabrication steps for LSCO nanowires described in the text. Adapted from reference [12].

robust to the Ar^+ ion milling process, it protect the film underneath the geometries during the etching process. Moreover, carbon can be easily removed by oxygen reactive ion etching. Then the carbon mask is covered with a double layer of electron-sensitive resist.

4. A electron-sensitive polymer resist is exposed to an electron beam in correspondence of the geometries. The interaction of the electron with the resist changes the polymer structural properties, such that it can be easily removed by soaking the sample in a chemical developer. In contrast, the unexposed resist will not be removed during the development.
5. A thin layer of chromium (Cr) is deposited on the sample, it will serve as protection for the carbon mask during the oxygen plasma etching.
6. The remaining resist is removed after the lift-off. At this point the carbon corresponding to the geometries is covered with chromium.
7. The carbon not covered by chromium is removed with oxygen plasma etching, and the mask is finally designed.
8. The geometries are transferred to the film with Ar^+ ion milling etching. The Au, the LSCO, and part of the substrate not covered by the carbon are etched away with an Ar^+ ion beam. This is the most critical step in the fabrication process. The beam current and voltage must be carefully calibrated to minimize the interaction between the ions and the nanostructures. We decided to set the beam voltage close to the etching threshold. The overheating of the nanowires is mitigated by the presence of gold, moreover the sample is glued on a metallic plate cooled with liquid nitrogen.
9. The remaining carbon is removed with another oxygen plasma etching and the nanowires are ready.

The key feature of this improved nanopatterning procedure is the addition of a gold capping layer between the film and the mask. The gold capping layer helps to

minimize the damages to the nanostructures during the fabrication process. Capping the nanowires with gold has a dual advantage: 1) due to the Au higher thermal conductivity than carbon it helps to mitigate the heating of the nanostructure during the ion argon milling step. Indeed, local overheating in cuprates causes oxygen-out-diffusion, degrading the superconducting properties of the nanostructure. 2) The Au layer also protect the surface of the nanowires during the O₂ plasma etching. It has been demonstrated that, in YBCO nanowires capped with gold, the theoretical GL limit for the depairing current can be reached [12]. On the other hand, it has never been possible to achieve this result in nanowires without gold capping due to the impurities and defects, introduced during the fabrication process, to which are subject uncapped nanowires. The value of the critical current density close to the GL theoretical limit is a clear indication of the high homogeneity and quality of the nanowires capped with gold.

5

Nanowires measurements

In this chapter we will present the results of the measurements of the nanowires, in terms of superconducting transition, current-voltage characteristic, value and temperature dependence of the critical current density J_c . First, the choice of the patterned film and the choice of the geometry of the nanowires will be discussed, then the results of the measurements will be presented.

5.1 Nanowire geometry and film used for the nanopatterning

Due to the high criticality of the nanofabrication process, and since it was the first time it has been applied to LSCO thin films at Chalmers, we decided to grow and to nanopattern a 50 nm thick film to avoid possible complication in the process. The film shows an onset of the critical temperature of about 26 K (shown in figure 5.1), lower than the one of the best film we obtained. However, the main objective of the fabrication part is to confirm the reliability of the nanofabrication process by investigating the quality of the nanowires. To this purpose it is not relevant if the film is optimally doped or not. On the contrary, since underdoped LSCO is even more sensitive to oxygen-out-diffusion, it represents the perfect benchmark to test the efficiency of the fabrication process. We realized nanowires of different width, from 50 to 500 nm. The width of the nanowire has been confirmed with the Scanning Electron Microscopy (SEM) after the lift-off (step 6 in chapter 4) to avoid possible contamination of the sample final devices caused by SEM imaging. A SEM image of one 200 nm wide nanowire after the lift-off is shown in figure 5.2. It is worth noting that the geometry of the nanowire has been designed in such a way to reduce current crowding effects. Indeed, in case of sharp angles between the bridge and the electrodes, the current density at the inner corners is enhanced compared to the average current density at the centre of the bridge. This causes the current density at the corner to reach the critical values while in the centre of the wire it is still below that limit. As a consequence, depending on the ratio between the inner corner bending radius and the bridge width, the current crowding can strongly reduce the average critical current density of the bridge, even for bridge whose width is smaller than the Pearl length [118].

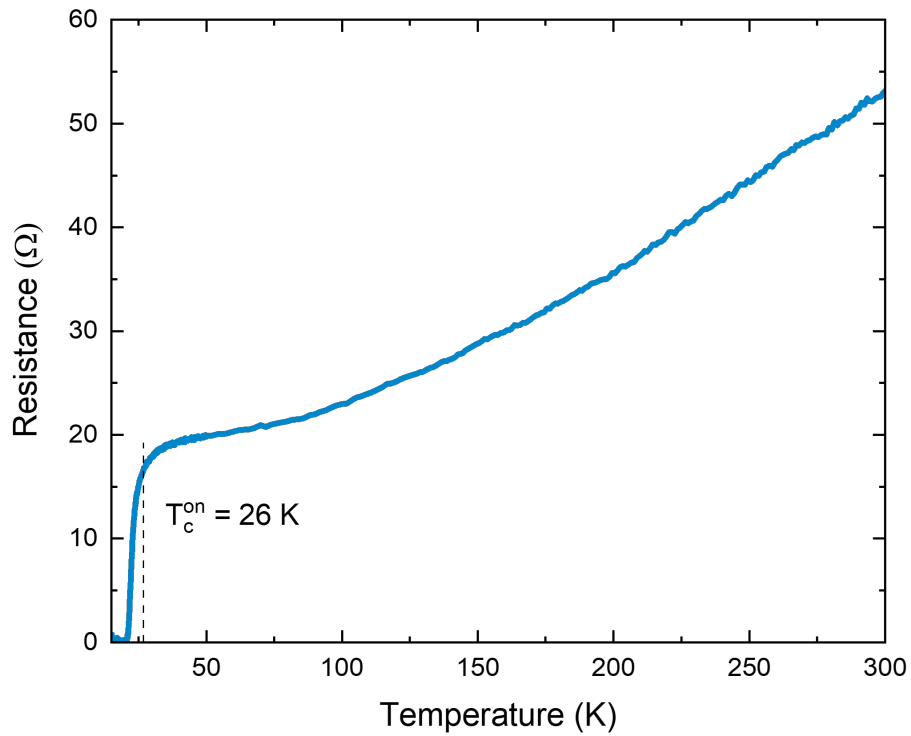


Figure 5.1: Resistance vs temperature measurement of the 50 nm thick film we used for the nanopatterning.

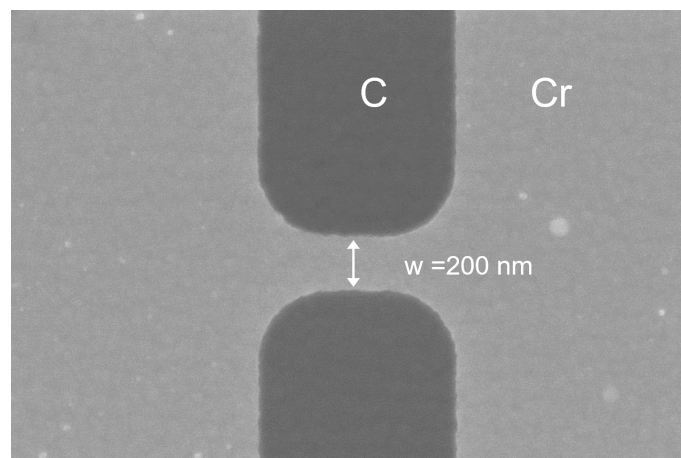


Figure 5.2: Scanning Electron Microscopy image of a 200 nm wide nanowire after the lift-off (step 6 in chapter 4). In order to avoid current crowding effect the angles of the nanowire are rounded.

5.2 Measurement setup

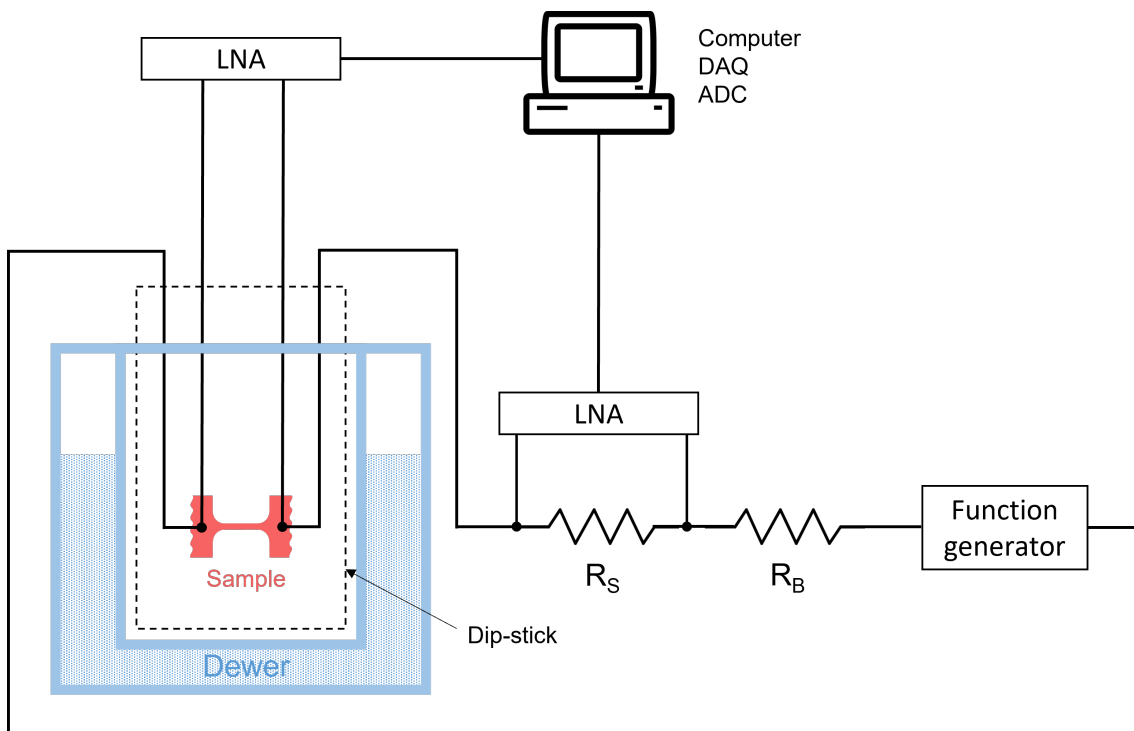


Figure 5.3: Schematics of the 4K dip-stick setup.

In figure 5.3 the schematics of the measurement setup is illustrated. The nanowires were measured with a ^4He 4K dip-stick system, equipped with 44 DC lines. The $5 \times 5 \text{ mm}^2$ sample is glued to a sample holder. The nanowires pads are bonded to the sample holder pads with an aluminium wire. To cool down the nanodevices, the sample holder is mounted in thermal contact with the ^4He pot located inside a dip-stick that is then inserted inside the ^4He dewar, surrounded by a superconducting magnetic shield. In this way the sample is cooled down to 4.2 K.

All the nanodevices are low-ohmic, with finite critical current. Therefore, the measurements are performed in current bias mode. A high ohmic resistance R_b is used to bias the device, while the current is measured indirectly with a resistor with lower resistance R_s . In order to minimize the digital noise, the cryostat and the Low Noise Amplifiers (LNA) are placed inside an electromagnetic interference shielded room, while all the electronics used for the measurements (function generator, analog to digital converters, data acquisition system, and the computer) is instead out of the shielded room. Finally, the signal is filtered by a LC filter.

5.3 Results

In this section the results of the measurements for the 50 and 500 nm wide nanowires will be presented. The devices were characterized in terms of resistance vs temperature superconducting transition, current-voltage characteristic, and temperature

dependence of the critical current density. We fabricated also nanowires of width 100, 200, 300 but due to the degradation of the carbon mask during the fabrication process, in the region where those devices were placed, they were damaged. For this reason, we could not measure these nanowires and we focus the discussion on 50 and 500 nm wide devices.

5.3.1 Resistivity vs temperature

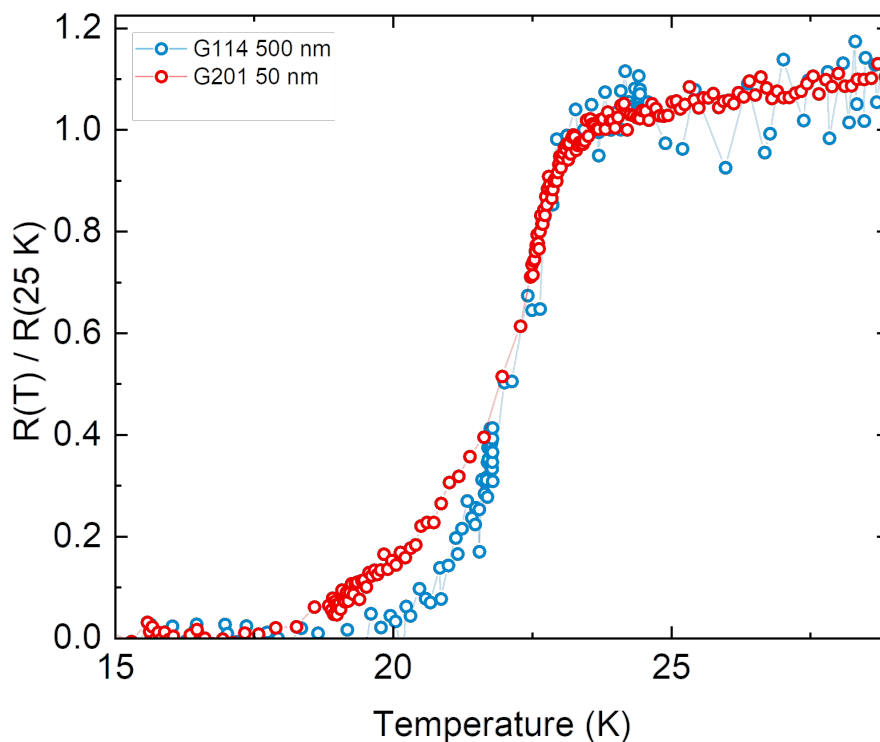


Figure 5.4: Resistance around the superconducting transition for a 50 and 500 nm width nanowire. It can be noticed that the the transition is broadened in both cases, but it is more pronounced in the narrowest nanowire.

We have measured the resistance of the 50 and 500 nm wide LSCO nanowires as a function of the temperature, from room temperature (~ 300 K) to 5 K. The results of the measurements, with a focus on the temperature range around the superconducting transition, are reported in figure 5.4. The current and voltage probes are located at the end of two wide and long electrodes, with width $w > 10^4$ nm and length $l > 10^5$ nm, connected at the nanowires. Therefore, the first transition at higher temperature is related to the electrodes, while at lower temperature the broader transition of the bridge occur (around ~ 23 K). It is worth noting that the first transition of the electrodes is ~ 2 K lower than the one of the bare film of LSCO. This is due to the Au capping layer that act as a shunt resistor, and not to

a degradation of the superconducting properties of the devices. The reason is the following: the measured resistance can be modeled as the parallel of two resistors, the LSCO nanowire $R_w(T)$, and the gold wire R_{Au} , therefore the total resistance will be $R(T)^{-1} = R_w^{-1}(T) + R_{Au}^{-1}$. The resistance of the gold is much smaller than the one of LSCO wire in the normal state, hence it becomes dominant at temperature close to T_c . Instead, when the temperature is low enough, the resistance of the LSCO nanowire will be smaller than the one of gold, dominating the total resistance and resulting in a "reduced" critical temperature.

Moreover, it can be noticed that the broadening of the transition for the narrowest nanowire is more pronounced than the for wider one. To understand the underlying reason we have to take into account the effect of thermal fluctuations. Indeed, in system with reduced dimensionality it can be observed that the superconducting phase transition is frequently not sharp, even in absence of any inhomogeneity. In 1D wires ($w, t \ll \xi$) this broadening is due to thermally activated phase slips (TAPS) that, having spacial extension of the order of the coherence length, hence of the wire diameter, disrupt locally the flow of supercurrent, resulting in a non-zero resistance of the wire [119–121]. Instead, in 3D wires ($w > 4.44\xi, l > 3.49\xi$), the resistive state is triggered by the Abrikosov vortices crossing the wire below T_c , even at low bias currents [46, 122, 123]. Both this models predict a transition broader in temperature for decreasing wire width, in complete agreement with our data. In particular, the energy barrier for the vortices crossing the wire is proportional to the width of the wire.

5.3.2 Current-voltage characteristics

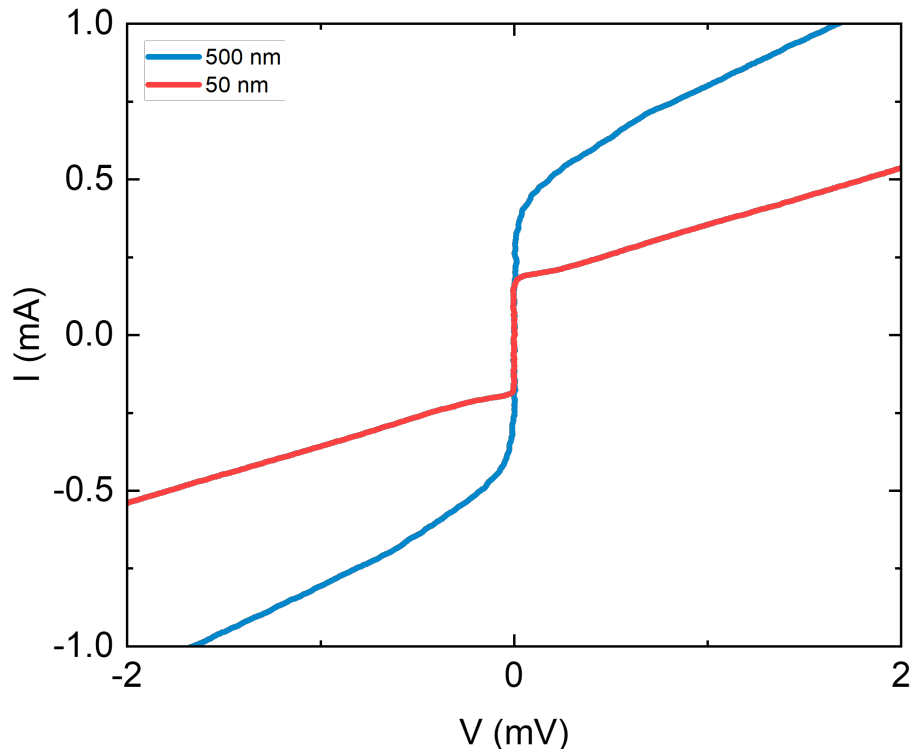


Figure 5.5: Current voltage characteristics for a 50 nm width wire, in blue, and a 500 nm width wire, in red.

In figure 5.5 the current-voltage characteristics (IVC) at 4.2 K of a 50 nm and a 500 nm width nanowires are presented. It can be noticed that the 50 nm wide nanowire present a flux-flow like IVC at high bias voltage, and then a small switch from zero voltage to a finite voltage state at lower bias. On the other hand, for the 500 nm wide nanowire the IVC is flux-flow like in the entire range of bias voltage. The origin of the small switch for the narrowest nanowire is still under investigation. However, it has been observed also in state-of-the-art YBCO nanowires of similar dimensions, where it has been proposed that this small switch could be associated to the vortex motion [12, 123].

From the IVC of the nanowire it has been possible to determine the critical current of the nanowires, with a voltage criterion of $20 \mu\text{V}$. From the value of the critical current I_c , the critical current density J_c has been determined as $J_c = I_c/wt$, where w and t are respectively the width and the thickness of the nanowire. The value of J_c for the 50 and 500 nm width nanowires are respectively $J_c^{50} = 6.9 \times 10^6 \text{ A/cm}^2$ and $J_c^{500} = 1.1 \times 10^6 \text{ A/cm}^2$. As expected the value for the critical current density of the narrowest nanowires is larger than for the wider one. The reason is that decreasing the width of the nanowire is possible to approach the GL theoretical limit for the depairing current density [13].

5.3.3 Temperature dependence of the critical current density

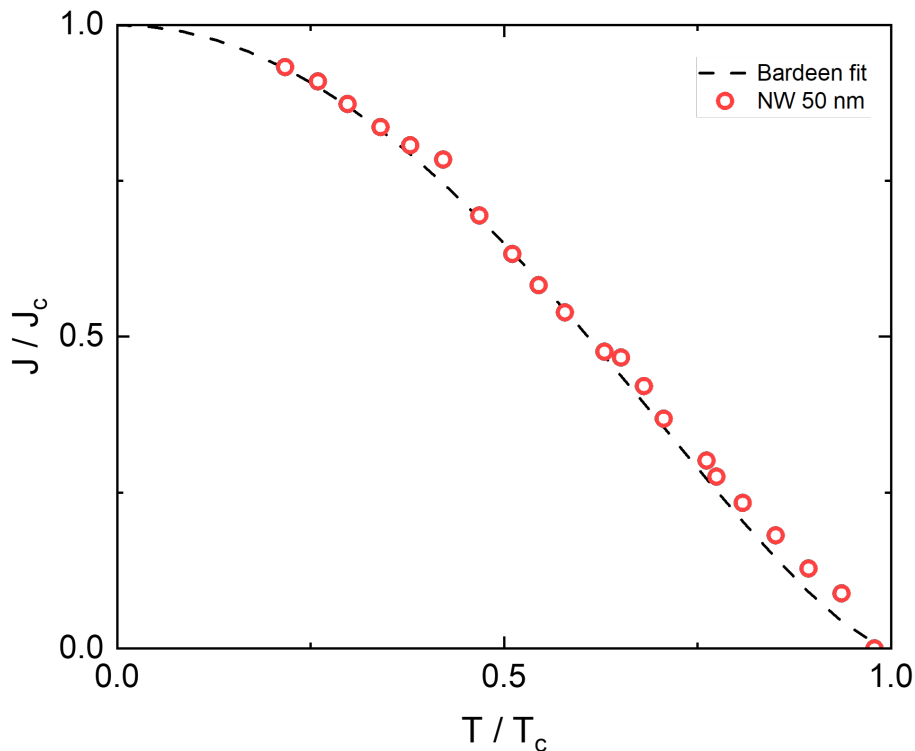


Figure 5.6: temperature dependence of the critical current density for a 50 nm width nanowire. The data are fitted with the Bardeen expression.

To further demonstrate the excellent quality of the 50 nm wide nanowires, in terms of uniformity of the transport properties, we have measured the temperature dependence of the critical current density (shown in figure 5.6), from 4.2 K up to the critical temperature T_c . The data are well fitted with the Bardeen expression [124], commonly used to describe low-temperature superconductors (LTS):

$$J_c(T) \propto J_c^0 \left[1 - \left(\frac{T}{T_c} \right)^2 \right]^{\frac{3}{2}} \quad (5.1)$$

where J_c^0 is the critical current density at temperature equal to zero. From the fit it has been possible to extrapolate the value of $J_c^0 = 7.7 \times 10^6$ A/cm² and of $T_c = 23.5$ K for our nanowires. As discussed in chapter 1.2 and 4, the J_c^0 value must be compared to the GL theoretical limit for the depairing current J_v due to vortex motion, representing the value for an ideal nanowire. For the calculation of the depairing current we used values of $\lambda = 500$ nm and $\xi = 3$ nm compatible with an underdoped LSCO with critical temperature of 23.5 K [5, 17], obtaining $J_v = 1.2 \times 10^7$ A/cm². Therefore, our nanowires show a value for the critical current

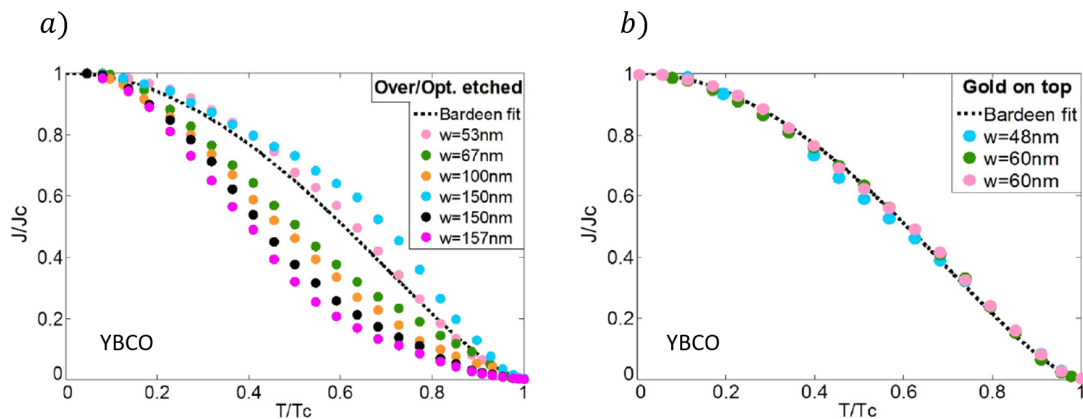


Figure 5.7: Normalized critical current density as a function of temperature for a) overetched and optimally etched YBCO nanowires, b) YBCO nanowires with a gold capping layers. From ref. [13].

density close (by a factor of ~ 1.5) to the theoretical GL limit. One possibility for the reason why our nanowires show a lower depairing current than the expected one could reside in the not perfectly optimized fabrication parameters. In particular, as already said the most delicate step is the Ar^+ ion etching. Although we used etching parameters that showed a good universality among other cuprates, it is likely that for LSCO it is required a further optimization to aim to perfectly homogeneous defects-free nanostructures. Another possibility could be that the quality of the film we used for the fabrication of nanowires was not perfect. Possible disorder in the film, induced by the strain or by some non-stoichiometry, may results in non perfect homogeneity of the transport properties, affecting the critical current density of the nanowires.

To further demonstrate the significance of our results we have compared the critical current density temperature dependence with state-of-the-art YBCO nanowires. Indeed, it has been demonstrated that the Bardeen-like J_c temperature dependence is a signature of the high-quality of the nanowires in terms of homogeneity of the bridge and uniformity of the transport properties [13]. In figure 5.7 the results obtained in previous work for YBCO nanowires are shown [13]. In particular, in figure 5.7a) the normalized J_c temperature dependence for optimally- and over- etched samples of different widths is illustrated, while in figure 5.7b) the normalized J_c temperature dependence for nanowires capped with gold is reported. It is immediate to notice that in the case of uncapped nanowires, where defects and impurities are introduced during the fabrication process, the $J_c(T)$ considerably deviates from the Bardeen expression. They show values of critical current density in temperature both above and below the expected ones. On the contrary, the agreement between the experimental data and the Bardeen expression is excellent for the Au capped nanowires. Moreover, the nanowires capped with gold show values of the critical current density very close to the GL depairing limit, further demonstrating the validity of the previous assessment, while it has not been possible to obtain the same results in un-

capped wires. Finally, also the reproducibility of the results is drastically increased in Au capped wires. Our results corroborate the quality of the fabrication process used for YBCO. Therefore, it is likely that the ultimate reason of the reduced J_c of our nanowires reside in the quality of the film rather than in the process itself. To understand the reason further experiments will be carried out.

However, this work represent an important step in the fabrication of LSCO nanostructures, and pave the way to obtain state-of-the-art LSCO nanowires with dimensions in the order of the nanometers, and with the superconducting properties of the pristine material.

6

Summary and outlook

The main focus of the thesis was the growth optimization of optimally doped LSCO ultra-thin film (15 u.c.) and their patterning into nanodevices. We have successfully grown optimally doped LSCO film with T_c comparable to the bulk one. The spread of the film T_c is most probably due to the quality of the substrate surface. Moreover, we succeeded in the fabrication of nanowires down to 50 nm width with transport properties comparable to the pristine material. The high degree of homogeneity of the nanowires has been demonstrated by comparing the critical current density values to the GL theoretical depairing limit, and by studying the temperature dependence of the critical current density. However, further optimization both of the film growth and of the fabrication process is required to achieve state-of-the-art LSCO nanodevices.

To conclude, we have worked on possible future research directions.

In order to reduce the spread of the growth results a particular attention must be focused on the substrate surface preparation. To this purpose we propose two possible methods to test and improve the quality of the substrate, and consequently of the films:

1. **Single terminated LSAO substrate.** It has been demonstrated that is possible to obtain single terminated LSAO surface, both (Sr,La)O (A-site) terminated or AlO_2 (B-site) terminated [125]. This can be done annealing the substrate in La-rich or in Al-rich environment respectively. Moreover, recent work on LSCO growth with MBE has shown how single-terminated B-site LSAO substrate are crucial to obtain state-of-the-art LSCO thin films [126].
2. **LSAO buffer layer.** Another possibility is to grow LSCO film on STO with a buffer layer of LSAO, thick enough to completely relax the strain. This method would have the advantages to grow in-situ both the LSAO buffer layer and the LSCO film, and to allow a higher degree of strain tunability of the film controlling the thickness of the LSAO buffer layer. On the other hand, in this way the control on the termination of the LSAO buffer surface would be missing.

After a further optimization of the growth conditions, the consequent step is to optimize the fabrication process for LSCO nanostructures. Considering the promising results obtained in this work, we strongly believe that this will not be the main challenge for future studies.

The next and most important step to take in this project is the realization of LSCO thin films as a function of the strontium doping, and their nanopatterning, to study the various intertwined orders in the underdoped regime and check how and if the strain affects the ground state. Finally, the bare underdoped LSCO films will be also

6. Summary and outlook

used for resonant inelastic x-ray scattering spectroscopy. This project in its entirety will possibly add a fundamental dowel to the puzzle of HTS, giving important hints to disclose not only the nature of this simple, but yet complex, material, but of the whole cuprates.

Bibliography

- [1] P. J. Ray, “Structural investigation of $\text{La}_{2-x}\text{Sr}_x\text{CuO}_{4+y}$,” Ph.D. thesis.
- [2] E. Wahlberg, “Reshaping the phase diagram of $\text{YBa}_2\text{Cu}_3\text{O}_{7-\delta}$ through strain in ultrathin films and nanowires,” Ph.D. thesis.
- [3] J. J. Wen *et al.*, “Observation of two types of charge-density-wave orders in superconducting $\text{La}_{2-x}\text{Sr}_x\text{CuO}_4$,” *Nat. Commun.*, vol. 10, no. 1, p. 3269, 2019.
- [4] H. Miao *et al.*, “Charge density waves in cuprate superconductors beyond the critical doping,” *npj Quantum Mater.*, vol. 6, no. 1, pp. 1–6, 2021.
- [5] T. P. Croft *et al.*, “Charge density wave fluctuations in $\text{La}_{2-x}\text{Sr}_x\text{CuO}_4$ and their competition with superconductivity,” *Phys. Rev. B*, vol. 89, no. 22, p. 224513, 2014.
- [6] K. A. Moler, “How the cuprates hid their stripes,” *Nature*, vol. 468, no. 7324, pp. 643–644, 2010.
- [7] H. Sato and M. Naito, “Increase in the superconducting transition temperature by anisotropic strain effect in (001) $\text{La}_{1.85}\text{Sr}_{0.15}\text{CuO}_4$ thin films on LaSrA10 4 substrates,” *Physica C: Supercond. Appl.*, p. 6, 1997.
- [8] H. Takagi *et al.*, “Superconductor-to-nonsuperconductor transition in $\text{La}_{2-x}\text{Sr}_x\text{CuO}_4$ as investigated by transport and magnetic measurements,” *Phys. Rev. B*, vol. 40, no. 4, pp. 2254–2261, 1989.
- [9] H. Sato *et al.*, “ $\text{La}_{2-x}\text{Sr}_x\text{CuO}_y$ epitaxial thin films ($x=0$ to 2): Structure, strain, and superconductivity,” *Phys. Rev. B*, vol. 61, pp. 12447–12456, 2000.
- [10] S. Hasegawa, “Reflection high-energy electron diffraction,” *Characterization of Materials*, vol. 97, pp. 1925–1938, 2012.
- [11] M. Naito *et al.*, “Epitaxial effects in thin films of high- T_c cuprates with the K_2NiF_4 structure,” *Physica C: Supercond. Appl.*, vol. 546, pp. 84–114, 2018.
- [12] R. Arpaia *et al.*, “Improved Nanopatterning for YBCO Nanowires Approaching the Depairing Current,” *IEEE Trans. Appl. Supercond.*, vol. 23, no. 3, pp. 1101505–1101505, 2013.
- [13] S. Nawaz *et al.*, “Approaching the theoretical depairing current in $\text{YBa}_2\text{Cu}_3\text{O}_{7-x}$ nanowires,” *Physica C: Supercond. Appl.*, vol. 495, pp. 33–38, 2013.

- [14] J. R. Waldram, ed., *Superconductivity of Metals and Cuprates*. Boca Raton: CRC Press, 1996.
- [15] Y. Wang and H. H. Wen, “Doping dependence of the upper critical field in $\text{La}_{2-x}\text{Sr}_x\text{CuO}_4$ from specific heat,” *EPL*, vol. 81, no. 5, p. 57007, 2008.
- [16] C. Panagopoulos *et al.*, “Effects of carrier concentration on the superfluid density of high- T_c cuprates,” *Phys. Rev. B*, vol. 60, no. 21, pp. 14617–14620, 1999.
- [17] T. Shibauchi *et al.*, “Anisotropic penetration depth in $\text{La}_{2-x}\text{Sr}_x\text{CuO}_4$,” *Phys. Rev. Lett.*, vol. 72, no. 14, pp. 2263–2266, 1994.
- [18] J. P. Franck *et al.*, “Copper and oxygen isotope effects in $\text{La}_{2-x}\text{Sr}_x\text{CuO}_4$,” *Phys. Rev. Lett.*, vol. 71, no. 2, pp. 283–286, 1993.
- [19] A. Beck *et al.*, “ $\text{La}_{1.85}\text{Sr}_{0.15}\text{CuO}_{4-\delta}$ bicrystal grain boundary Josephson junctions,” *Appl. Phys. Lett.*, vol. 68, no. 23, pp. 3341–3343, 1996.
- [20] Q. Li *et al.*, “Magnetic penetration depth of $(\text{La}_{1-x}\text{Sr}_x)_2\text{CuO}_4$ single crystals,” *Phys. Rev. B*, vol. 47, no. 5, pp. 2854–2860, 1993.
- [21] J. G. Bednorz and K. A. Muller, “Possible high- T_c superconductivity in the BaLaCuO system,” *Z. Phys. B*, vol. 64, no. 2, pp. 189–193, 1986.
- [22] B. Keimer *et al.*, “From quantum matter to high-temperature superconductivity in copper oxides,” *Nature*, vol. 518, no. 7538, pp. 179–186, 2015.
- [23] G. Ghiringhelli *et al.*, “Long-Range Incommensurate Charge Fluctuations in $(\text{Y,Nd})\text{Ba}_2\text{Cu}_3\text{O}_{6+x}$,” *Science*, vol. 337, no. 6096, pp. 821–825, 2012.
- [24] E. H. da Silva Neto *et al.*, “Ubiquitous Interplay Between Charge Ordering and High-Temperature Superconductivity in Cuprates,” *Science*, vol. 343, no. 6169, pp. 393–396, 2014.
- [25] J. M. Tranquada *et al.*, “Evidence for unusual superconducting correlations coexisting with stripe order in $\text{La}_{1.875}\text{Ba}_{0.125}\text{CuO}_4$,” *Phys. Rev. B*, vol. 78, no. 17, p. 174529, 2008.
- [26] C. V. Parker *et al.*, “Fluctuating stripes at the onset of the pseudogap in the high- T_c superconductor $\text{Bi}_2\text{Sr}_2\text{CaCu}_2\text{O}_{8+x}$,” *Nature*, vol. 468, no. 7324, pp. 677–680, 2010.
- [27] J. Chang *et al.*, “Direct observation of competition between superconductivity and charge density wave order in $\text{YBa}_2\text{Cu}_3\text{O}_{6.67}$,” *Nature Phys.*, vol. 8, no. 12, pp. 871–876, 2012.
- [28] B. Lake *et al.*, “Antiferromagnetic order induced by an applied magnetic field in a high-temperature superconductor,” *Nature*, vol. 415, no. 6869, pp. 299–302, 2002.
- [29] N. F. Mott and R. Peierls, “Discussion of the paper by de Boer and Verwey,” *Proc. Phys. Soc.*, vol. 49, no. 4S, pp. 72–73, 1937.

-
- [30] J. M. Tranquada *et al.*, “Evidence for stripe correlations of spins and holes in copper oxide superconductors,” *Nature*, vol. 375, no. 6532, pp. 561–563, 1995.
- [31] B. Yu *et al.*, “Unusual Dynamic Charge Correlations in Simple-Tetragonal $\text{HgBa}_2\text{CuO}_{4+\delta}$,” *Phys. Rev. X*, vol. 10, no. 2, p. 021059, 2020.
- [32] G. Seibold *et al.*, “Strange metal behaviour from charge density fluctuations in cuprates,” *Commun. Phys.*, vol. 4, no. 1, pp. 1–6, 2021.
- [33] S. Caprara *et al.*, “Dissipation-driven strange metal behavior,” *Commun. Phys.*, vol. 5, no. 1, pp. 1–7, 2022.
- [34] J. P. Locquet *et al.*, “Doubling the critical temperature of $\text{La}_{1.9}\text{Sr}_{0.1}\text{CuO}_4$ using epitaxial strain,” *Nature*, vol. 394, no. 6692, pp. 453–456, 1998.
- [35] I. Sochnikov *et al.*, “Large oscillations of the magnetoresistance in nanopatterned high-temperature superconducting films,” *Nat. Nanotechnol.*, vol. 5, no. 7, pp. 516–519, 2010.
- [36] N. E. Litombe *et al.*, “ $\text{La}_{2-x}\text{Sr}_x\text{CuO}_4$ superconductor nanowire devices,” *Physica C: Supercond. Appl.*, vol. 506, pp. 169–173, 2014.
- [37] H. K. Onnes, “The resistance of pure mercury at helium temperatures,” *Commun. Phys. Lab. Univ. Leiden*, p. 120, 1911.
- [38] W. Meissner and R. Ochsenfeld, “Ein neuer Effekt bei Eintritt der Supraleitfähigkeit,” *Naturwissenschaften*, vol. 21, no. 44, pp. 787–788, 1933.
- [39] F. London *et al.*, “The electromagnetic equations of the superconductor,” *Proc. Math. Phys. Eng. Sci.*, vol. 149, no. 866, pp. 71–88, 1935.
- [40] Landau, L. D. and Ginzburg, V. L., “On the theory of superconductivity,” *Zh. Eksp. Teor. Fiz.*, vol. 1064, p. 20, 1950.
- [41] A. A. Abrikosov, “On the magnetic properties of superconductors of the second group,” *Sov. Phys. JETP*, vol. 5, pp. 1174–1182, 1957.
- [42] J. Bardeen, L. N. Cooper, and J. R. Schrieffer, “Theory of Superconductivity,” *Phys. Rev.*, vol. 108, no. 5, pp. 1175–1204, 1957. Publisher: American Physical Society.
- [43] K. F. Herzfeld *et al.*, “Isotope Effect and Lattice Properties in Superconductivity,” *Phys. Rev.*, vol. 79, no. 5, pp. 911–911, 1950.
- [44] M. Tinkham, *Introduction to Superconductivity*. Courier Corporation, 2004.
- [45] D. Y. Vodolazov *et al.*, “Modulation instability of the order parameter in thin-film superconductors with edge barrier,” *EPL*, vol. 48, no. 3, p. 313, 1999.
- [46] L. N. Bulaevskii *et al.*, “Vortex-induced dissipation in narrow current-biased thin-film superconducting strips,” *Phys. Rev. B*, vol. 83, no. 14, p. 144526, 2011.
- [47] R. J. Cava *et al.*, “Bulk superconductivity at 36 K in $\text{La}_{1.8}\text{Sr}_{0.2}\text{CuO}_4$,” *Phys. Rev. Lett.*, vol. 58, no. 4, pp. 408–410, 1987.

- [48] M. K. Wu *et al.*, “Superconductivity at 93 K in a new mixed-phase Y-Ba-Cu-O compound system at ambient pressure,” *Phys. Rev. Lett.*, vol. 58, no. 9, pp. 908–910, 1987.
- [49] A. Schilling *et al.*, “Superconductivity above 130 K in the Hg–Ba–Ca–Cu–O system,” *Nature*, vol. 363, no. 6424, pp. 56–58, 1993.
- [50] G. F. Sun *et al.*, “Tc enhancement of $\text{HgBa}_2\text{Ca}_2\text{Cu}_3\text{O}_{8+\delta}$ by Tl substitution,” *Phys. Lett. A*, vol. 192, no. 1, pp. 122–124, 1994.
- [51] D. J. Van Harlingen, “Phase-sensitive tests of the symmetry of the pairing state in the high-temperature superconductors - Evidence for $d_{x^2-y^2}$ symmetry,” *Rev. Mod. Phys.*, vol. 67, no. 2, pp. 515–535, 1995.
- [52] Z. X. Shen *et al.*, “Anomalously large gap anisotropy in the a-b plane of $\text{Bi}_2\text{Sr}_2\text{CaCu}_2\text{O}_{8+\delta}$,” *Phys. Rev. Lett.*, vol. 70, no. 10, p. 1553, 1993.
- [53] J. M. Tarascon *et al.*, “Superconductivity at 40 K in the Oxygen-Defect Perovskites $\text{La}_{2-x}\text{Sr}_x\text{CuO}_4$,” *Science*, vol. 235, no. 4794, pp. 1373–1376, 1987.
- [54] R. B. van Dover *et al.*, “Composition-dependent superconductivity in $\text{La}_{2-x}\text{Sr}_x\text{CuO}_{4+\delta}$,” *Phys. Rev. B*, vol. 35, no. 10, pp. 5337–5339, 1987.
- [55] J. D. Jorgensen *et al.*, “Structural properties of oxygen-deficient $\text{YBa}_2\text{Cu}_3\text{O}_{7-\delta}$,” *Phys. Rev. B*, vol. 41, no. 4, pp. 1863–1877, 1990.
- [56] C. Chaillout *et al.*, “The crystal structure of superconducting $\text{La}_2\text{CuO}_{4.032}$ by neutron diffraction,” *Physica C: Supercond. Appl.*, vol. 158, no. 1, pp. 183–191, 1989.
- [57] S. Kanbe *et al.*, “Superconductivity and Lattice Parameters in $(\text{La}_{1-x}\text{Sr}_x)_2\text{CuO}_{4-\delta}$ Solid Solution System,” *Chem. Lett.*, vol. 16, no. 3, pp. 547–550, 1987.
- [58] I. Bozovic *et al.*, “Epitaxial Strain and Superconductivity in $\text{La}_{2-x}\text{Sr}_x\text{CuO}_4$ Thin Films,” *Phys. Rev. Lett.*, vol. 89, no. 10, p. 107001, 2002.
- [59] R. Liang *et al.*, “Evaluation of CuO_2 plane hole doping in $\text{YBa}_2\text{Cu}_3\text{O}_{6+x}$ single crystals,” *Phys. Rev. B*, vol. 73, no. 18, p. 180505, 2006. Publisher: American Physical Society.
- [60] J. B. Torrance *et al.*, “Properties that change as superconductivity disappears at high-doping concentrations in $\text{La}_{2-x}\text{Sr}_x\text{CuO}_4$,” *Phys. Rev. B*, vol. 40, no. 13, pp. 8872–8877, 1989.
- [61] M. R. Presland *et al.*, “General trends in oxygen stoichiometry effects on T_c in Bi and Tl superconductors,” *Phys. C: Supercond. Appl.*, vol. 176, no. 1, pp. 95–105, 1991.
- [62] R. Arpaia *et al.*, “Probing the phase diagram of cuprates with $\text{YBa}_2\text{Cu}_3\text{O}_{7-\delta}$ thin films and nanowires,” *Phys. Rev. Materials*, vol. 2, no. 2, p. 024804, 2018.
- [63] A. A. Abrikosov, *Fundamentals of the Theory of Metals*. Courier Dover Publications, 2017.

-
- [64] A. Kaminski *et al.*, “Crossover from Coherent to Incoherent Electronic Excitations in the Normal State of $\text{Bi}_2\text{Sr}_2\text{CaCu}_2\text{O}_{8+\delta}$,” *Phys. Rev. Lett.*, vol. 90, no. 20, p. 207003, 2003.
- [65] S. Martin *et al.*, “Normal-state transport properties of $\text{Bi}_{2+x}\text{Sr}_{2-y}\text{CuO}_{6+\delta}$ crystals,” *Phys. Rev. B*, vol. 41, no. 1, pp. 846–849, 1990.
- [66] K. Takenaka *et al.*, “Incoherent charge dynamics of $\text{La}_{2-x}\text{Sr}_x\text{CuO}_4$ Dynamical localization and resistivity saturation,” *Phys. Rev. B*, vol. 68, no. 13, p. 134501, 2003.
- [67] C. M. Varma *et al.*, “Phenomenology of the normal state of Cu-O high-temperature superconductors,” *Phys. Rev. Lett.*, vol. 63, no. 18, pp. 1996–1999, 1989.
- [68] Subir Sachdev, *Quantum Phase Transitions*. Cambridge Univ. Press, 1999.
- [69] B. Michon *et al.*, “Thermodynamic signatures of quantum criticality in cuprate superconductors,” *Nature*, vol. 567, no. 7747, pp. 218–222, 2019.
- [70] B. J. Ramshaw *et al.*, “Quasiparticle mass enhancement approaching optimal doping in a high- T_c superconductor,” *Science*, vol. 348, no. 6232, pp. 317–320, 2015.
- [71] S. Nakamae *et al.*, “Electronic ground state of heavily overdoped nonsuperconducting $\text{La}_{2-x}\text{Sr}_x\text{CuO}_4$,” *Phys. Rev. B*, vol. 68, no. 10, p. 100502, 2003.
- [72] D. S. Marshall *et al.*, “Unconventional Electronic Structure Evolution with Hole Doping in $\text{Bi}_2\text{Sr}_2\text{CaCu}_2\text{O}_{8+\delta}$: Angle-Resolved Photoemission Results,” *Phys. Rev. Lett.*, vol. 76, no. 25, pp. 4841–4844, 1996.
- [73] M. R. Norman *et al.*, “The pseudogap: friend or foe of high- T_c ?,” *Adv. Phys.*, vol. 54, no. 8, pp. 715–733, 2005.
- [74] W. E. Pickett, “Electronic structure of the high-temperature oxide superconductors,” *Rev. Mod. Phys.*, vol. 61, no. 2, pp. 433–512, 1989.
- [75] M. Hashimoto *et al.*, “Energy gaps in high-transition-temperature cuprate superconductors,” *Nature Phys.*, vol. 10, no. 7, pp. 483–495, 2014.
- [76] H.-B. Yang *et al.*, “Emergence of preformed Cooper pairs from the doped Mott insulating state in $\text{Bi}_2\text{Sr}_2\text{CaCu}_2\text{O}_{8+\delta}$,” *Nature*, vol. 456, no. 7218, pp. 77–80, 2008.
- [77] H. Takagi *et al.*, “Systematic evolution of temperature-dependent resistivity in $\text{La}_{2-x}\text{Sr}_x\text{CuO}_4$,” *Phys. Rev. Lett.*, vol. 69, no. 20, pp. 2975–2978, 1992.
- [78] T. Ito *et al.*, “Systematic deviation from T-linear behavior in the in-plane resistivity of $\text{YBa}_2\text{Cu}_3\text{O}_{7-\delta}$: Evidence for dominant spin scattering,” *Phys. Rev. Lett.*, vol. 70, no. 25, pp. 3995–3998, 1993.
- [79] N. Barišić *et al.*, “Universal sheet resistance and revised phase diagram of the cuprate high-temperature superconductors,” *Proc. Natl. Acad. Sci. U.S.A.*, vol. 110, no. 30, pp. 12235–12240, 2013.

- [80] J. L. Tallon and J. W. Loram, “The doping dependence of T^* – what is the real high- T_c phase diagram?,” *Phys. C: Supercond. Appl.*, vol. 349, no. 1, pp. 53–68, 2001.
- [81] F. Laliberté *et al.*, “Origin of the metal-to-insulator crossover in cuprate superconductors,” arXiv:1606.04491.
- [82] R. A. Cooper *et al.*, “Anomalous Criticality in the Electrical Resistivity of $\text{La}_{2-x}\text{Sr}_x\text{CuO}_4$,” *Science*, vol. 323, no. 5914, pp. 603–607, 2009.
- [83] Y. Kohsaka *et al.*, “Visualization of the emergence of the pseudogap state and the evolution to superconductivity in a lightly hole-doped Mott insulator,” *Nature Phys.*, vol. 8, no. 7, pp. 534–538, 2012.
- [84] Y. Sato *et al.*, “Thermodynamic evidence for a nematic phase transition at the onset of the pseudogap in $\text{YBa}_2\text{Cu}_3\text{O}_y$,” *Nature Phys.*, vol. 13, no. 11, pp. 1074–1078, 2017.
- [85] B. Fauqué *et al.*, “Magnetic Order in the Pseudogap Phase of High- T_c Superconductors,” *Phys. Rev. Lett.*, vol. 96, no. 19, p. 197001, 2006.
- [86] M. Le Tacon *et al.*, “Inelastic X-ray scattering in $\text{YBa}_2\text{Cu}_3\text{O}_{6.6}$ reveals giant phonon anomalies and elastic central peak due to charge-density-wave formation,” *Nature Phys.*, vol. 10, no. 1, pp. 52–58, 2014.
- [87] H. H. Wu *et al.*, “Charge stripe order near the surface of 12-percent doped $\text{La}_{2-x}\text{Sr}_x\text{CuO}_4$,” *Nat. Commun.*, vol. 3, no. 1, p. 1023, 2012.
- [88] S. Blanco-Canosa *et al.*, “Resonant x-ray scattering study of charge-density wave correlations in $\text{YBa}_2\text{Cu}_3\text{O}_{6+x}$,” *Phys. Rev. B*, vol. 90, no. 5, p. 054513, 2014.
- [89] R. Comin *et al.*, “Charge Order Driven by Fermi-Arc Instability in $\text{Bi}_2\text{Sr}_{2-x}\text{La}_x\text{CuO}_{6+\delta}$,” *Science*, vol. 343, no. 6169, pp. 390–392, 2014.
- [90] H. Miao *et al.*, “High-temperature charge density wave correlations in $\text{La}_{1.875}\text{Sr}_{0.125}\text{CuO}_4$ without spin-charge locking,” *Proc. Natl. Acad. Sci. U.S.A.*, vol. 114, no. 47, pp. 12430–12435, 2017.
- [91] R. Arpaia *et al.*, “Dynamical charge density fluctuations pervading the phase diagram of a Cu-based high- T_c superconductor,” *Science*, vol. 365, no. 6456, pp. 906–910, 2019.
- [92] R. Arpaia and G. Ghiringhelli, “Charge Order at High Temperature in Cuprate Superconductors,” *J. Phys. Soc. Jpn.*, vol. 90, no. 11, p. 111005, 2021.
- [93] Q. Li *et al.*, “Two-Dimensional Superconducting Fluctuations in Stripe-Ordered $\text{La}_{1.875}\text{Ba}_{0.125}\text{CuO}_4$,” *Phys. Rev. Lett.*, vol. 99, no. 6, p. 067001, 2007.
- [94] D. F. Agterberg *et al.*, “The Physics of Pair-Density Waves: Cuprate Superconductors and Beyond,” *Annu. Rev. Condens. Matter Phys.*, vol. 11, no. 1, pp. 231–270, 2020.

- [95] S. D. Edkins *et al.*, “Magnetic field–induced pair density wave state in the cuprate vortex halo,” *Science*, vol. 364, no. 6444, pp. 976–980, 2019.
- [96] E. Fradkin *et al.*, “Colloquium: Theory of intertwined orders in high temperature superconductors,” *Rev. Mod. Phys.*, vol. 87, no. 2, pp. 457–482, 2015.
- [97] H. Huang *et al.*, “Two-Dimensional Superconducting Fluctuations Associated with Charge-Density-Wave Stripes in $\text{La}_{1.87}\text{Sr}_{0.13}\text{Cu}_{0.99}\text{Fe}_{0.01}\text{O}_4$,” *Phys. Rev. Lett.*, vol. 126, no. 16, p. 167001, 2021.
- [98] S. Yomo *et al.*, “High Pressure Study and the Critical Current of High- T_c Superconductor $(\text{La}_{0.9}\text{Sr}_{0.1})_2\text{CuO}_{4-y}$,” *Jpn. J. Appl. Phys.*, vol. 26, no. 5A, p. L603, 1987.
- [99] M. Suzuki, “Hall coefficients and optical properties of $\text{La}_{2-x}\text{Sr}_x\text{CuO}_4$ single-crystal thin films,” *Phys. Rev. B*, vol. 39, no. 4, pp. 2312–2321, 1989.
- [100] H. L. Kao *et al.*, “In situ growth and properties of single-crystalline-like $\text{La}_{2-x}\text{Sr}_x\text{CuO}_4$ epitaxial films by off-axis sputtering,” *Appl. Phys. Lett.*, vol. 59, pp. 2748–2750, Nov. 1991.
- [101] M. Z. Cieplak *et al.*, “Thickness dependence of $\text{La}_{2-x}\text{Sr}_x\text{CuO}_4$ films,” *Appl. Phys. Lett.*, vol. 65, no. 26, pp. 3383–3385, 1994.
- [102] T. L. Meyer *et al.*, “Strain-relaxation and critical thickness of epitaxial $\text{La}_{1.85}\text{Sr}_{0.15}\text{CuO}_4$ films,” *APL Mater.*, vol. 3, no. 12, p. 126102, 2015.
- [103] H. Sato *et al.*, “Growth of (001) $\text{La}_{1.85}\text{Sr}_{0.15}\text{CuO}_4$ ultrathin films without buffer or cap layers,” *Physica C: Supercond. Appl.*, vol. 274, no. 3-4, pp. 227–231, 1997.
- [104] B. O. Wells *et al.*, “Incommensurate Spin Fluctuations in High-Transition Temperature Superconductors,” *Science*, vol. 277, no. 5329, pp. 1067–1071, 1997.
- [105] X. Leng and I. Božović, “Controlling Superconductivity in $\text{La}_{2-x}\text{Sr}_x\text{CuO}_{4+\delta}$ by Ozone and Vacuum Annealing,” *J. Supercond. Nov. Magn.*, vol. 28, no. 1, pp. 71–74, 2015.
- [106] R. Rakshit *et al.*, “Influence of buffer layers on superconductivity in $\text{La}_{1.85}\text{Sr}_{0.15}\text{CuO}_4$ epitaxial films,” *Physica C Supercond.*, vol. 415, no. 1-2, pp. 74–78, 2004.
- [107] I. E. Trofimov *et al.*, “Growth and properties of $\text{La}_{2-x}\text{Sr}_x\text{CuO}_4$ films,” *Appl. Phys. Lett.*, vol. 65, no. 19, pp. 2481–2483, 1994.
- [108] W. Si and X. X. Xi, “Growth and properties of pulsed laser deposited superconducting $\text{La}_{1.85}\text{Sr}_{0.15}\text{CuO}_4$ thin films,” *IEEE Trans. Appl. Supercond.*, vol. 9, no. 2, pp. 2406–2409, 1999.
- [109] S. Trommler *et al.*, “Preparation of epitaxial $\text{La}_{2-x}\text{Sr}_x\text{CuO}_4$ thin films for dynamic investigations of epitaxial strain,” *J. Phys.: Conf. Ser.*, vol. 234, no. 1, p. 012045, 2010.

- [110] N. Auvray *et al.*, “Nematic fluctuations in the cuprate superconductor $\text{Bi}_2\text{Sr}_2\text{CaCu}_2\text{O}_{8+\delta}$,” *Nat. Commun.*, vol. 10, no. 1, p. 5209, 2019.
- [111] H. H. Kim *et al.*, “Uniaxial pressure control of competing orders in a high-temperature superconductor,” *Science*, vol. 362, no. 6418, pp. 1040–1044, 2018.
- [112] K. Cho *et al.*, “Using controlled disorder to probe the interplay between charge order and superconductivity in NbSe_2 ,” *Nat. Commun.*, vol. 9, no. 1, p. 2796, 2018.
- [113] E. Wahlberg *et al.*, “Restored strange metal phase through suppression of charge density waves in underdoped $\text{YBa}_2\text{Cu}_3\text{O}_{7-\delta}$,” *Science*, vol. 373, no. 6562, pp. 1506–1510, 2021.
- [114] S. Das *et al.*, “Structural, magnetic, and superconducting properties of pulsed-laser-deposition-grown $\text{La}_{1.85}\text{Sr}_{0.15}\text{CuO}_4/\text{La}_{2/3}\text{Ca}_{1/3}\text{MnO}_3$ superlattices on (001)-oriented LaSrAlO_4 substrates,” *Phys. Rev. B*, vol. 89, no. 9, p. 094511, 2014.
- [115] R. Baghdadi *et al.*, “Fabricating Nanogaps in $\text{YBa}_2\text{Cu}_3\text{O}_{7-\delta}$ for Hybrid Proximity-Based Josephson Junctions,” *Phys. Rev. Applied*, vol. 4, no. 1, p. 014022, 2015.
- [116] R. Baghdadi *et al.*, “Toward $\text{YBa}_2\text{Cu}_3\text{O}_{7-\delta}$ Nanoscale Structures for Hybrid Devices,” *IEEE Trans. Appl. Supercond.*, vol. 25, no. 3, pp. 1–4, 2015. Conference Name: IEEE Transactions on Applied Superconductivity.
- [117] S. Charpentier *et al.*, “Hot spot formation in electron-doped PCCO nanobridges,” *Phys. Rev. B*, vol. 94, no. 6, p. 060503, 2016.
- [118] S. Nawaz *et al.*, “Microwave Response of Superconducting $\text{YBa}_2\text{Cu}_3\text{O}_{7-\delta}$ Nanowire Bridges Sustaining the Critical Depairing Current: Evidence of Josephson-like Behavior,” *Phys. Rev. Lett.*, vol. 110, no. 16, p. 167004, 2013.
- [119] W. A. Little, “Decay of Persistent Currents in Small Superconductors,” *Phys. Rev.*, vol. 156, no. 2, pp. 396–403, 1967.
- [120] J. S. Langer and V. Ambegaokar, “Intrinsic Resistive Transition in Narrow Superconducting Channels,” *Phys. Rev.*, vol. 164, no. 2, pp. 498–510, 1967.
- [121] D. E. McCumber and B. I. Halperin, “Time Scale of Intrinsic Resistive Fluctuations in Thin Superconducting Wires,” *Phys. Rev. B*, vol. 1, no. 3, pp. 1054–1070, 1970.
- [122] M. Bell *et al.*, “One-dimensional resistive states in quasi-two-dimensional superconductors: Experiment and theory,” *Phys. Rev. B*, vol. 76, no. 9, p. 094521, 2007.
- [123] R. Arpaia *et al.*, “Resistive state triggered by vortex entry in $\text{YBa}_2\text{Cu}_3\text{O}_{7-\delta}$ nanostructures,” *Physica C: Supercond. Appl.*, vol. 506, pp. 165–168, 2014.

- [124] J. Bardeen, “Critical Fields and Currents in Superconductors,” *Rev. Mod. Phys.*, vol. 34, no. 4, pp. 667–681, 1962.
- [125] A. Biswas *et al.*, “Selective A- or B-site single termination on surfaces of layered oxide SrLaAlO₄,” *Appl. Phys. Lett.*, vol. 102, p. 051603, Feb. 2013. Publisher: American Institute of Physics.
- [126] X. Xu *et al.*, “Synthesis of La_{2-x}Sr_xCuO₄ films via atomic layer-by-layer molecular beam epitaxy,” *APL Materials*, vol. 10, no. 6, p. 061103, 2022.

A

Appendix 1

The recipe of the nanopatterning procedures presented here are tailored for the Nanofabrication Laboratory at the Department of Microtechnology and Nanoscience, Chalmers. As a consequence, the used parameters are optimized for the equipment available there.

A.0.0.1 LSCO nanowires

1. **Film deposition:** a 50 nm thick LSCO film is deposited by PLD on LaSrAlO₄ (001) oriented.
2. **Au capping layer:** the film is coated with a 50 nm thick gold layer deposited by magnetron sputtering deposition at a deposition rate of 7-8 Å/sec.
3. **Hard carbon mask deposition:** a 100 nm thick hard carbon mask is deposited by PLD at a deposition rate of 3 Å/sec. To improve the adherence of the carbon layer, the deposition starts at low laser energy and it is then increased after ~ 30 sec.
4. **E-resist coating:** a double layer of electron beam polymer resist (e-resist) is spin-coated on top of the sample. The bottom layer is MMA co-polymer EL4, and the top layer is ARP6200:IPA 1:3. Both are spinned at 6000 rpm and baked for 5 min at 95 °C.
5. **Electron beam lithography:** the CAD mask file is exposed with the e-beam JEOL JBX 9300FS system. The electron acceleration voltage is 100 kV. For the small features (e.g. nanowires bridge) a current of 2 nA is used, while for the big structures (e.g. electrodes) a current of 35 nA is used. In both cases the dose used is 210 $\mu\text{C}/\text{cm}^2$.
6. **E-resist development:** the e-resists are developed at room temperature in o-Xylene 96% (top layer) and in MIBK:IPA 1:3 (bottom layer), both for 35 sec.
7. **Cr deposition:** a thin layer of chromium (12 nm) is deposited on the sample by electron beam physical vapor deposition, at a rate of 1 Å/sec.
8. **Lift-off:** the remaining e-resist is lift-off in 1165 developer, warmed at 60 °C, for 10 min.
9. **Reactive Ion Etching (RIE):** the unprotected C layer is removed by O₂ plasma RIE for 20 min at 50 W, and pressure 100 mTorr.
10. **Ar⁺ ion milling:** the C mask geometry is transferred to the sample by LN₂ cooled Ar⁺ ion milling. This is the most delicate and important step of the fabrication, therefore we report the critical parameters in table A.1.

Parameter	value
V_{beam} [V]	300
I_{beam} [mA]	2
J_{beam} [$\mu\text{A}/\text{cm}^2$]	30
I_{neutr} [mA]	50
Ar ₊ ion flow [sccm]	5
Stage tilt [°]	5
Stage rotation	ON

Table A.1: Ar⁺ ion milling parameters.

11. **RIE:** the remaining carbon is removed by another O₂ plasma RIE for 18 min, with the same parameter of step 9.

DEPARTMENT OF MICROTECHNOLOGY AND NANOSCIENCE
CHALMERS UNIVERSITY OF TECHNOLOGY
Gothenburg, Sweden
www.chalmers.se



CHALMERS
UNIVERSITY OF TECHNOLOGY